STRUCTURE AND ELECTROCHEMICAL PROPERTIES OF TITANIUM DOPED SPINEL MANGANESE OXIDE

Paradron Lektrakoontara

A Thesis Submitted in Partial Fulfillment of the Requirements for the

Degree of Master of Science in Chemistry

Suranaree University of Technology

Academic Year 2016

โครงสร้างและสมบัติทางเคมีไฟฟ้าของสปิเนลแมงกานีสออกไซด์เจือไทเทเนียม

นายภราดร เล็กตระกูลธารา

วิทยานิพนธ์นี้เป็นส่วนหนึ่งของการศึกษาตามหลักสูตรปริญญาวิทยาศาสตรมหาบัณฑิต
สาขาวิชาเคมี
มหาวิทยาลัยเทคโนโลยีสุรนารี
ปีการศึกษา 2559

STRUCTURE AND ELECTROCHEMICAL PROPERTIES OF TITANIUM DOPED SPINEL MANGANESE OXIDE

Suranaree University of Technology has approved this thesis submitted in partial fulfillment of the requirements for a Master's Degree.

Thesis Examining Committee

(Prof. Dr. Jatuporn Wittayakun)
Chairperson

Theeranun Siritanon
(Asst. Prof. Dr. Theeranun Siritanon)
Member (Thesis Advisor)

Rapee Utke
(Assoc. Prof. Dr. Rapee Utke)
Member

(Asst. Prof. Dr. Sanchai Prayoonpokarach)
Member

(Prof. Dr. Santi Maensiri)
Vice Rector for Academic Affairs
and Internationalization

(Asst. Prof. Dr. Worawat Meevasana)
Dean of Institute of Science

ภราดร เล็กตระกูลธารา : โครงสร้างและสมบัติทางเคมีไฟฟ้าของสปิเนลแมงกานีสออกไซด์เจือไทเทเนียม (STRUCTURE AND ELECTROCHEMICAL PROPERTIES OF TITANIUM DOPED SPINEL MANGANESE OXIDE) อาจารย์ที่ปรึกษา : ผู้ช่วยศาสตราจารย์ ดร.ธีรนันท์ ศิริตานนท์, 71 หน้า.

งานวิจัยนี้ได้ศึกษาผลของไทเทเนียมต่อโครงสร้าง องค์ประกอบทางเคมี สัณฐานวิทยา พื้นที่ผิว เลขออกซิเดชัน และพฤติกรรมทางไฟฟ้าเคมีของแมงกานีสออกไซด์ สปิเนลแมงกานีสออกไซด์เจือไทเทเนียมสังเคราะห์ด้วยวิธีทำปฏิกิริยาระหว่างกรดกับ LiMn$_{2-x}$Ti$_x$O$_4$ โดยสารละลายของแข็งของ LiMn$_{2-x}$Ti$_x$O$_4$ (x = 0 0.25 0.5 0.75 และ 1) สามารถสังเคราะห์ได้ด้วยวิธีการทำปฏิกิริยาสถานะของแข็ง จากการศึกษาพบว่า การแทนที่โลหะแมงกานีสด้วยโลหะไทเทเนียมส่งผลเล็กน้อยต่อสัณฐานวิทยาและพื้นที่ผิว แต่ส่งผลกระทบต่อโครงสร้างอย่างมีนัยสำคัญซึ่งมีบทบาทสำคัญต่อพฤติกรรมทางเคมีไฟฟ้า โดยใช้ไซคลิกโวแทมเมทรีศึกษาคุณสมบัติทางเคมีไฟฟ้า ทั้งนี้การเก็บประจุของผลิตภัณฑ์ถูกแยกออกเป็นการเก็บประจุที่ผิวและภายใน โดยอาศัยการปรับอัตราเร็วการเปลี่ยนแปลงศักย์ไฟฟ้า แม้ว่าการเก็บประจุที่ผิวจะลดลงอย่างต่อเนื่องเมื่อปริมาณของโลหะแมงกานีสลดลง แต่โครงสร้างของสารส่งผลต่อการเก็บประจุภายใน การมีอยู่ของไทเทเนียมในแมงกานีสออกไซด์ช่วยเพิ่มขนาดหน่วยเซลล์และเหนี่ยวนำให้แมงกานีสและไทเทเนียมบางส่วนไปอยู่ในตำแหน่ง 16c และ 8a ตามลำดับ โดยแมงกานีสและไทเทเนียมในตำแหน่งดังกล่าวจะลดการแพร่ผ่านของไอออนเข้าสู่ภายในโครงสร้าง ในขณะที่การขยายตัวของหน่วยเซลล์จะช่วยเพิ่มโอกาสการแทรกตัวของไอออนเข้าไปในโครงสร้างของวัสดุ ทำให้ความสามารถในการเก็บประจุของสารตัวอย่างที่มี x = 0.25 ถึง 0.75 เพิ่มตามปริมาณไทเทเนียมในโครงสร้าง

สาขาวิชาเคมี
ปีการศึกษา 2559

ลายมือชื่อนักศึกษา ภราดร เล็กตระกูลธารา
ลายมือชื่ออาจารย์ที่ปรึกษา ธีรนันท์ ศิริตานนท์

PARADRON LEKTRAKOONTARA : STRUCTURE AND
ELECTROCHEMICAL PROPERTIES OF TITANIUM DOPED SPINEL
MANGANESE OXIDE. THESIS ADVISOR :
ASST. PROF. THEERANUN SIRITANON, Ph.D. 71 PP.

SUPERCAPACITOR/OXIDES/CAPACITIVE ELEMENTS/ACID LEACHING

The effect of Ti on structure, chemical composition, morphology, surface area, oxidation state and electrochemical behavior of spinel MnO_2 have been investigated. Solid solutions of $LiMn_{2-x}Ti_xO_4$ (x = 0, 0.25, 0.5, 0.75 and 1) were synthesized by solid state reaction. To obtain Ti doped MnO_2, deintercalation of $LiMn_{2-x}Ti_xO_4$ was achieved by acid treatment. Replacing Mn with Ti has little effect on the morphology and surface area but significantly affect the crystallographic structure which is found to play important roles in determining the electrochemical behaviors. Cyclic voltammetry is used to study the electrochemical properties. Capacitive elements of the products were separated to surface capacitance and insertion capacitance by varying scan speeds. Although the surface capacitances generally decrease when the number of Mn active species decrease, the change in insertion capacitance is affected by crystallographic structure of the compounds. The presence of Ti in MnO_2 increases lattice parameter and induces Mn and Ti to occupy in the 16c and 8a site, respectively.

The presence of Mn and Ti in the mentioned site reduces ion diffusion into bulk material. On the other hand, the increase of lattice parameters could improve ion intercalation. Therefore, the specific capacitance increase with Ti content in the samples with x = 0.25 to x = 0.75.

School of Chemistry
Student's Signature ภราดร เลิศตระกูลสวาง

Academic Year 2016
Advisor's Signature Theeranun Siritanon

ACKNOWLEDGEMENTS

I would like to thank my thesis supervisor, Asst. Prof. Dr. Theeranun Siritanon, for her helpful, supportive advices and support throughout the thesis and the writing of this thesis.

I also would like to acknowledge the committee including Prof. Dr. Jatuporn Wittayakun, Assoc. Prof. Dr. Rapee Utke and Asst. Prof. Dr. Sanchai Prayoonpokarach for all of their guidance through this thesis.

Lastly, I would like to thank my scholarship, Development and Promotion of Science and Technology Talents Project (Royal Government of Thailand scholarship), for financial supports.

Paradron Lektrakoontara

CONTENTS

Page

CHAPTER

CONTENTS (Continued)

Page

CONTENTS (Continued)

LIST OF TABLES

Table **Page**

LIST OF FIGURES

Figure **Page**

LIST OF FIGURES (Continued)

Figure **Page**

LIST OF FIGURES (Continued)

Figure **Page**

CHAPTER I

INTRODUCTION

1.1 Introduction

Electrochemical capacitors (ECs) or supercapacitors become the promising device for energy storage applications due to its high power density, high cycle performance and fast recharging process. Cathode is one of the important parts of supercapacitors which affects their performance and electrical capacity. Several materials such as carbon, conducting polymers and metal oxides have been studied as possible cathode materials. Charge storage of supercapacitors is based on two mechanisms: electric double layer capacitance (EDLC) which is an electrolytic charge accumulation at electrode surfaces and pseudocapacitance which is related to redox reactions of active materials.

At present, metal oxides have been focused on in electrode materials development due to their high specific capacitance (Zhi *et al*., 2013; Zhang *et al*., 2009). The highest capacitance was found on RuO_2 but its cost and toxicity have limited RuO_2 in commercial production (Zhang *et al*., 2009). Recently, many researchers are interested in MnO_2 for electrode materials due to its low cost, environmental compatibility and good electrochemical behavior. Unfortunately, despite the high theoretical capacitance, it was reported in literatures that experimental specific capacitance of MnO_2 is only about 100 F g^{-1} for powder and 700 F g^{-1} for thin film owing to electrode corrosion and lack of electronic and ionic conductivity (Ghodbane *et al*., 2009).

There are several factors which affect specific capacitance of materials such as morphology (Mao *et al*., 2012), pore structure (Luo *et al*., 2007), pore diameter (Sawangphruk *et al*., 2012), synthesis method (Zhi *et al*., 2013; Subramanian *et al*., 2005), specific surface area and particle size. Additional factors include electrode preparation such as loading method and loading mass (Wan *et al*., 2014).

Interestingly, MnO_2 has several possible crystallographic structures. Each structure is constructed with MnO_6 octahedral building block in various arrangements presenting 1D, 2D and 3D structure with different tunnel size. Devaraj *et al*. (2008) and Grobane *et al*. (2009) studied electrochemical behavior of MnO_2 with different crystal structure. They found that each structure gives different capacitance value. It was found that there are two significant factors affecting the capacitance; the specific surface area and the ionic conductivity. Ionic conductivity of each structure is related to its tunnel. High ionic conductivity is observed in structures with large channel size. Therefore, MnO_2 with large tunnel size tends to present higher specific capacitance. Interestingly, spinel MnO_2, whose structure consists of relatively small channels for ion diffusion, exhibits unexpectedly high ionic conductivity and specific capacitance. Thus, it is concluded that not only the size, but also the connectivity of such channels plays important roles in determining the capacitance of MnO_2 (Ghodbane *et al*., 2009).

The current research aims to further study the effects of channel size on the electrochemical behavior of spinel MnO_2. Titanium is chosen as the doped metal to enlarge unit cell and expand the size of three-dimensional interconnected channel in MnO_2 spinel lattice. The relationship between the composition, structure and electrochemical properties of Ti-doped MnO_2 is discussed. The obtained results are believed to be useful in deepening the understanding of charge storage mechanisms of related oxides.

CHAPTER II

LITERATURE REVIEW

Capacitor is a well-known charge storage device used in many applications such as automobiles, aircraft and space, medicine, computers and power supply circuits. Leiden jar, the first technology of capacitor was developed by Pieter van Musschenbroek in 1745 (Jayalakshmi and Balasubramanian, 2008).

2.1 Types of capacitors

2.1.1 Electrostatic capacitors

An electrostatic capacitor or conventional capacitor is a basic and first generation of capacitors. Today, conventional capacitors comprise of two parallel metallic electrodes placed in mutual opposition and separated by dielectric materials or insulators such as paper, water, paraffin, polymer and air. (Figure 2.1)

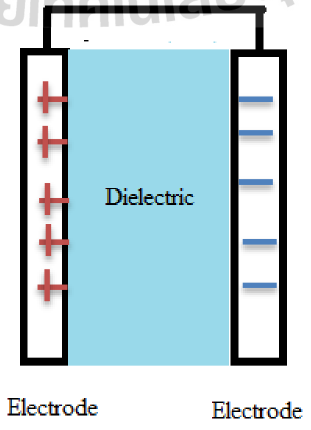

Figure 2.1 Basic configuration of electrostatic capacitor.

Charge storage principle can be descripted as follow: when voltage is applied between 2 electrodes, electrons on the metallic plate from one side will be driven to the other plate. In this case, electrons will flow from low to high potential until the potential between two plates are equal to that of the applied one. As a result, positive charges occur on the metallic plate which losses electrons and negative charges will be stored on the other plate. After that, the applied voltage is cut off. This described process is called a charging process. When capacitors are used, electrons from the rich-electron electrode will be released and flowed back to the deficient-electron electrode until charges between two electrodes are balanced. (Figure 2.2)

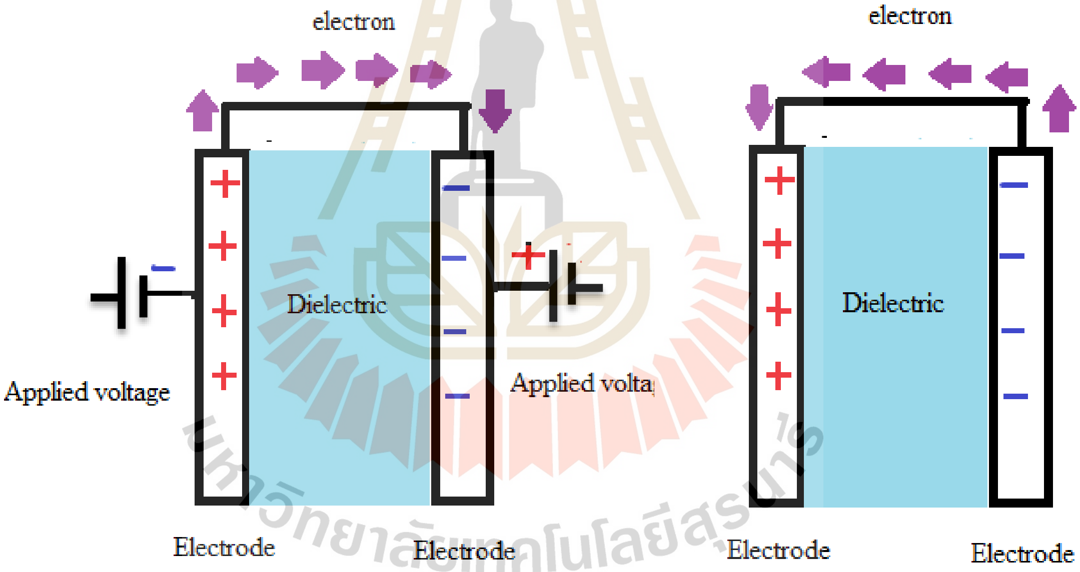

Figure 2.2 Charging process (left) and discharging process (right) of an electrostatic capacitor.

Generally, capacitance of electrostatic capacitors is in the range of 0.1 to 1 μF in a voltage range of 50 to 400 V. Capacity of conventional capacitors is explained by equation (2.1) where C is electrostatic capacity (μF), ε is dielectric constant, A is surface area of the electrode (cm^2) and d is thickness of dielectric (cm)

$$C = \varepsilon A/d \tag{2.1}$$

In an electrical circuit, when capacitors are connected to other capacitors or components, the equivalent capacitance can be calculated by equation (2.2) and (2.3) when the capacitors are connected in parallel and series configuration, respectively. C_{eq} is an equivalent capacitance.

$$C_{eq} = C_1 + C_2 + \ldots + C_n \tag{2.2}$$

$$C_{eq} = 1/C_1 + 1/C_2 + \ldots + 1/C_n \tag{2.3}$$

Electrode materials of electrostatic capacitors such as silicon usually gives low capacitances. Its capacitance could be increased by using insulator materials with a high permittivity and effective surface areas. Surface area of silicon-based electrodes could be increased by etching process (Jayalakshmi and Balasubramanian, 2008).

2.1.2 Electrolytic capacitor

An electrolytic capacitor is the second generation of capacitors. The capacitance of electrolytic capacitors is improved by the use of dielectric oxides with increased ε value. The configuration of electrolytic capacitors consists of a cathode foil, an anode foil, a dielectric film and an electrolyte. A dielectric film is fabricated at surface of a cathode foil by anodizing process (Figure 2.3). There are many kinds of electrolytic capacitors depending on types of electrodes, dielectrics and electrolyte.

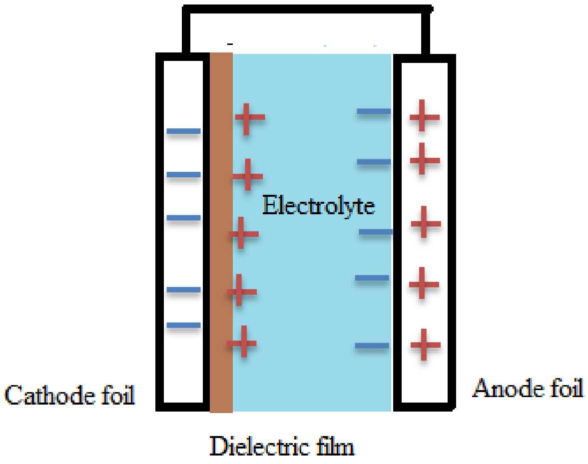

Figure 2.3 Basic configuration of electrolytic capacitor.

Charge storage mechanism of electrolytic capacitors is based on the double layer capacitance. Electrons are stored at electrode surface and stabilized by positive charge of the electrolyte. To demonstrate on how electrons flow in electrolytic capacitor, basic schematic electrical circuit showing basic components in capacitors is shown in Figure 2.4. C is the capacitance, R_{ESR} is the equivalent series resistance, L_{ESL} is the equivalent series inductance and R_{leak} is the resistance from leakage current.

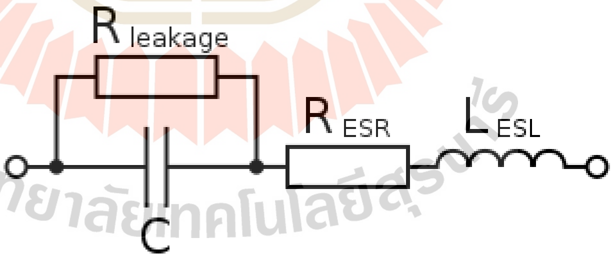

Figure 2.4 Basic schematic electrical circuit of electrolytic capacitor.

The commercial Ta capacitors use Ta_2O_5 as a dielectric film. Sulfuric acid is used as electrolyte for a wet type. Organic electrolytes such as polyaniline, polypyrrole and ethylene carbonate are used as an electrolyte for solid type. Its capacitances are in range of 0.1 to 10 µF. Like electrostatic capacitors, Ta capacitors are improved by increasing the effective area.

Additionally, there are ceramic capacitors constructed from layers of metals and ceramics. Ag-Pd and other metals such as Mn and Ca are used as electrodes and many types of ceramics are used as dielectrics such as $BaTiO_3$, $CaZrO_3$, $MgTiO_3$ and $SrTiO_3$. Their capacitance is in a range of 10 µF.

Besides oxide compounds and ceramics, the other types of electrolytic capacitors are film capacitors which use polyester and polypropylene as dielectric film and metal-glazed capacitors (Jayalakshmi and Balasubramanian, 2008).

2.2 Supercapacitors

Supercapacitors or ultracapacitors are high performance capacitors. According to Table 2.1 and Ragone plot in Figure 2.5, supercapacitors could store more energy than electrostatic capacitors and have more power density than batteries which fulfills the gap between conventional capacitors and batteries. Because of its properties, supercapacitors are used in many applications which require high energy and power such as engine start or acceleration for electric vehicles, backup power sources and energy storage devices (Zhang *et al*., 2009). Capacitance, energy (E) and power (P_{max}) of supercapacitors are calculated from equation (2.4), (2.5) and (2.6), respectively. Q is the collected charges in coulomb, C is the capacitance in Farads, V is voltage, and R is the equivalent series resistance in ohms. (Liu and Zhua, 2007).

$$C = Q/V \tag{2.4}$$

$$E = CV^2/2 \tag{2.5}$$

$$P_{max} = V^2/4R \tag{2.6}$$

Table 2.1 Properties of battery, electrostatic capacitors and supercapacitors (Zhang *et al.*, 2009).

Criteria	Battery	Electrostatic capacitors	Supercapacitors
Discharge time	0.3-3 h	10^{-3} to 10^{-6} s	0.3-30 s
Charge time	1-5 h	10^{-3} to 10^{-6} s	0.3-30 s
Energy density (Wh/Kg)	10-100	<0.1	1-10
Specific power (W/Kg)	50-200	>10,000	1000
Charge-discharge efficiency	0.7-0.85	1	0.85-0.98
Cycle life	500-2000	>500,000	>100,000

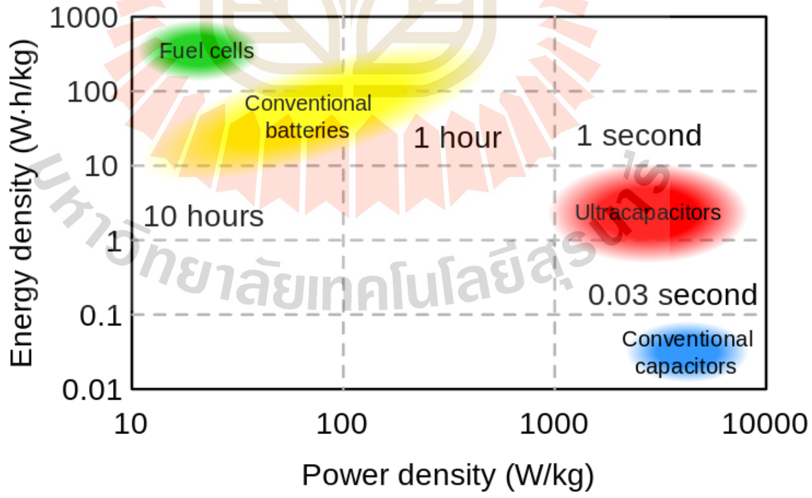

Figure 2.5 Ragone plot reveals power density and energy density of many types of energy storage devices (Stan, 2014).

Basic configuration of a supercapacitor consists of two electrodes, an electrolyte and a separator. Generally, separators are used to decrease ion movement speed in electrolyte solution in order to avoid short circuit (Figure 2.6).

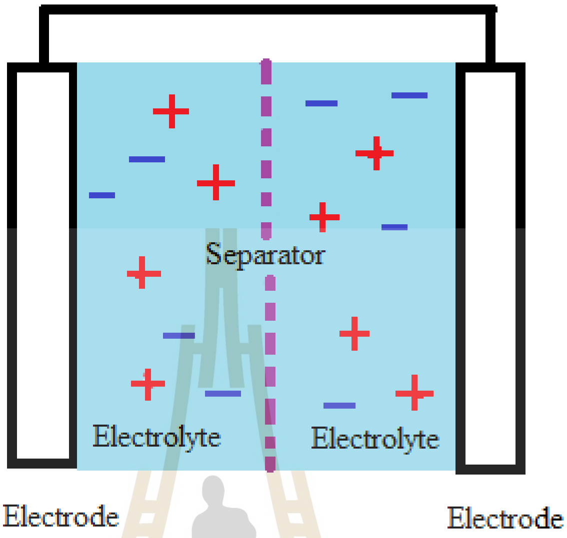

Figure 2.6 Basic configuration of a supercapacitor.

Comparing to batteries, supercapacitors store electrical charges only at surface rather than the entire electrodes. Types of supercapacitors are simply classified to electrical double layer capacitors (EDLC) and electrochemical capacitors (Pseudocapacitor) based on its charge storage character.

Charge storage of supercapacitors is similar to that of electrostatic capacitors. In charging process, the voltage is applied and electrons are stored at the electrode, positive and negative charges arise at electrodes and the opposite charges of electrolyte built up at electrode surface to locally neutralize electrical charge forming a Helmholtz layer. In a discharging process, electrons are released to generate electrical current and charged species in an electrolyte at the electrode surface would flow back to the electrolyte bulk (Figure 2.7).

Besides the double layer capacitance, some materials such as metal oxides could additionally have faradaic capacitance, called pseudocapacitance by reacting with the electrolyte and storing electrons in the form of chemical reactions.

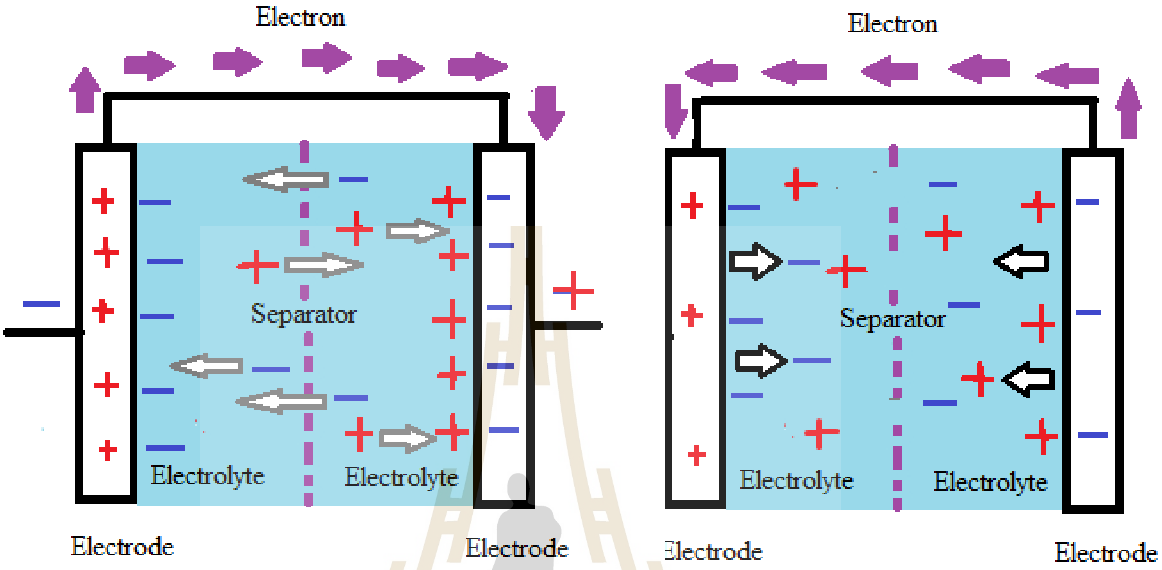

Figure 2.7 Charging process (left) and discharging process (right) of supercapacitors.

A single electron transfer is discussed here as equation (2.7) and (2.8). M is an electroactive material, X^+ is cation species in the electrolyte, A^- is anion, MC and MA are the obtained species. Both cation and anion in electrolyte could react with an electroactive material depending on the nature of materials and the types of ions. Typically, cations like H^+ and alkali ion such as Li^+, Na^+ and K^+ are used while anions such as Cl^-, Br^-, I^- and SCN^- are electron donating group (Zhang *et al.*, 2009).

$$M + A^- \longrightarrow MA + e^- \quad (2.7)$$

$$M + X^+ + e^- \longrightarrow MC \quad (2.8)$$

2.2.1 Electrical double layer capacitor (EDLC)

Theoretically, electrical double layer capacitors store electric charges only by a double layer mechanism. As a result, capacitance of EDLC is affected by number of charge accumulated on electrode surfaces. Therefore, the development of EDLC is based on increasing the specific surface area (Jayalakshmi and Balasubramanian, 2008). Carbon is a dominant material for EDLC electrodes because of the large surface area, high conductivity, low cost, non-toxicity and high stability. Several types of carbon have been investigated as summarized in Table 2.2 (Zhang *et al.*, 2009).

In reality, the key for high capacitance is not only specific areas of carbon materials but also carbon structure, pore size, particle size, electrical conductivity and surface functionalities (Pandolfo and Hollenkamp, 2006). Additionally, capacitance of nanoporous carbons depends on its matching degree to the applied electrolytes rather than its overall pore volume (Liu and Zhua, 2007).

Table 2.2 Examples of carbon-based materials for EDLC electrode (Zhang *et al.*, 2009).

Carbon-based material	Electrolyte	Working voltage (V)	Specific capacitance (F g^{-1})
Activated carbon (AC)	1 M Et_4NBF_4 + PC	1.5	40
Graphite	1 M Et_4NBF_4 + PC	3.0	12
Carbon aerogel	1.5 M Et_3MeNBF_4 + PC	3.0	160
Mesoporous carbon	30 wt% KOH	0.9	180
Meso/macroporous carbon	6 M KOH	0.8	130
C_{60}-loaded AC fiber	0.5 M H_2SO_4	1.0	172
Single-wall CNTs	EMITFSI	2.3	50
Multi-wall CNTs sheet	1.96 M $TEMABF_4$ + PC	2.5	13

*PC = poly carbonate, $TEMABF_4$ = Triethylmethylaammoniumtetrafluoroborate and EMITFSI = 1-Ethyl-3-methylimidazolium bis(trifluoromethylsulfonyl)imide.

2.2.2 Electrochemical capacitor (pseudocapacitor)

Charge storage principle of pseudocapacitors is based on both double layer capacitance and faradaic process providing more capacitances than EDLC. Many types of transition metal oxide compounds have been investigated as electrode materials for pseudocapacitors such as RuO_2, $Ni(OH)_2$, Fe_3O_4, WC, V_2O_5, SnO_2 and MnO_2as summarized in Table 2.3 (Zhang *et al.*, 2009).

Table 2.3 Examples of transition metal oxide compounds for pseudocapacitor electrodes (Zhang *et al.*, 2009).

Transition metal oxide compound	Electrolyte	Working voltage (V)	Specific capacitance (F g^{-1})
RuO_2 H_2O	0.5 M H_2SO_4	1.0	650
RuO_2 /carbon	PVA hydrogel	0.8	1000
MnO_2	0.5 M K_2SO_4	0.8	261
SnO_2/carbon aerogel	1 M H_2SO_4	1.0	68
$Ni(OH)_2$	3% KOH	0.8	578
Cobalt-nickel oxide/ CNTs	1 M KOH	1.0	569
WC/carbon	1 M H_2SO_4	0.9	477
TiN	1 M KOH	0.2	238
V_2O_5	2 M KCl	0.7	262

According to Table 2.3, RuO_2 seems to be the best material because of its high specific capacitance, long cycle life, high conductivity, and good electrochemical reversibility. However, the high cost, low abundance and toxicity limit the commercial uses of RuO_2. To surpass these limitations, other transition metal oxide compounds have been investigated.

2.3 Manganese oxide

Manganese oxide or manganese (IV) oxide (MnO_2) is blackish or brown solid found naturally in pyrolusite mineral. MnO_2 is used in many applications including as an essential component in dry-cell batteries such as Zn-carbon battery, a pigment, a catalyst for alcohol oxidation and a precursor for other manganese compounds such as $KMnO_4$. Moreover, MnO_2 is considerably cheaper and less toxic than most chemicals.

2.3.1 Crystal structures of MnO_2

Structure of MnO_2 consists of octahedral building block of six atoms of oxygen and one atom of manganese as shown in Figure 2.8. The difference of edge sharing and corner sharing of this octahedral building block leads to several crystal structures of $MnO_2$with different tunnel size. The MnO_2 is named by two main systems: the common name and the geek alphabet one as shown in Table 2.4.

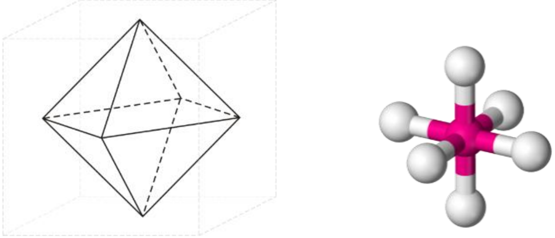

Figure 2.8 Octahedral building block of MnO_2: pink atom is manganese and white atom is oxygen (Eni, 2017; Ben, 2006).

Table 2.4 Nomenclature and several crystal structures of MnO_2 (Ghodbane *et al.*, 2009).

Geek alphabet	Common name	Crystal structure	Tunnel size
α	Cryptomelane		(2x2)
β	Pyrolusite		(1x1)
γ	Ramsdellite	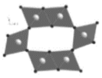	(1x2)
δ	Birnessite	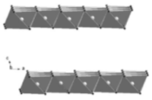	Inter layers
ε	-	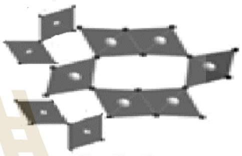	(1x1)(1x2)
λ	Spinel	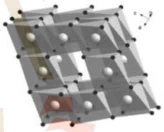	3D channel
-	Romanechite	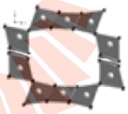	(2x3)
-	OMS-5	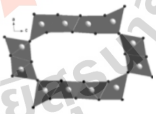	(2x4)
-	Todorokite	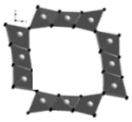	(3x3)
-	Wooddruffite	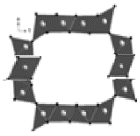	(3x4)

2.3.2 Electrochemical behavior of MnO_2

Recently, manganese oxide has attracted much attention as a material for supercapacitor electrodes because of its low cost, electrochemical behavior and environment compatibility. Generally, pseudocapacitance mechanism of MnO_2 is based on single-electron transfer reaction. According to equation (2.9) where X^+ is alkali cation such as Li^+, Na^+ and K^+; charges are stored in the form of faradaic reaction between cation and MnO_2. When MnO_2 is completely reduced from Mn^{4+} to Mn^{3+}, its specific capacitance would be 1233 F g^{-1} which is close to that of RuO_2 (Zhang *et al*., 2009)

$$MnO_2 + X^+ + e^- \longrightarrow MnOOX \tag{2.9}$$

However, MnO_2 suffers from its low electronic conductivity and corrosive effect. Many literatures report that experimental specific capacitance of MnO_2 is only about 100 F g^{-1} for powder and 700 F g^{-1} for thin film which is far from the theoretical value and not yet enough for commercial applications (Ghodbane *et al*., 2009).

In principle, there are 2 processes contributing to MnO_2 capacitance which are double layer capacitance and pseudocapacitance. Moreover, pseudocapacitance can be divided into two capacitive elements which are pseudocapacitive faradaic capacitance of MnO_2 surface (surface capacitance) and faradaic reaction of MnO_2 center requiring cation insertion/deinsertion (insertion capacitance). The surface capacitance occurs at outer surface of materials while insertion/deinsertion capacitance occurs at inner surface. Scan rate dependence of the current is used to separate each capacitive element. Equation (2.10) shows relation of the current as a function of scan rate when i(V) is the current at a given voltage, v is scan rate, k_1 and k_2 are scan rate dependent constants of surface capacitance and intercalation process.

$$i(V) = k_1 v + k_2 v^{1/2} \quad (2.10)$$

As these two processes occur at different rates, Trasatti *et al.* (1990) developed a method to quantitatively separate capacitive elements. They proposed that if sufficient time is given, all electrochemical process scan take place and the capacitance at scan rate at 0 mV s^{-1} will demonstrate the total capacitance (C_{tot}). On the other hand, the capacitance at scan rate infinity will demonstrate only surface capacitance (C_{sur}). Then, the insertion capacitance can be obtained from the difference between total capacitance and surface capacitance (C_{tot} - C_{sur}). Therefore, the certain number of C_{tot} and C_{sur} can be obtained by extrapolation of specific capacitance value at semi linear range from plot of specific capacitance as a function of $v^{1/2}$ and $v^{-1/2}$, respectively.

Both the surface and the insertion capacitance are important in determining electrochemical behaviors of MnO_2. While the surface capacitance significantly depends on the surface area and morphology, several works have shown that crystallographic structures of MnO_2 have great impact on the insertion one.

Sang *et al.* (2011) synthesized nanowire/nanorod α-MnO_2, urchins γ-MnO_2 and nanoplates δ-MnO_2 via persulfate treatment of divalent manganese compound at room temperature. Specific surface area and specific capacitance of each compound are presented in Table 2.5. The capacitive behavior can occur via two mechanisms which are adsorption/desorption of cations on its surface and intercalation/deintercalation into manganese lattice. The result showed that δ-MnO_2 is favorable for both mechanisms. Because it has the largest surface area compared to the others MnO_2 which increase surface capacitance, and the 2D layered structure provides a large channel size which allows more ion intercalation. However, γ-MnO_2 which has neither 2D interlayer structure nor channel available for cation shows a larger capacitance than α-MnO_2 due to a greater adsorption process from its larger specific surface. It was found that α-MnO_2 nanorod with a larger specific surface area has more specific capacitance than α-MnO_2 nanowires.

Table 2.5 Comparison between specific area and capacitance of several types of MnO_2.

Type of MnO_2 and its morphology	Crystal structure	Specific surface area (m^2 g^{-1})	Specific capacitance (F g^{-1})
δ-MnO_2 nanoplates	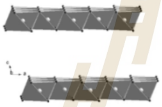	116	213
γ-MnO_2 urchins	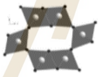	82	142
α-MnO_2 nanowires		53	110
α-MnO_2 nanorods		84	120

Chen *et al.* (2016) investigated the phase transformation of MnO_2 crystal structure from β-phase to α-phase inducing by doping Ce^{3+}. MnO_2 is prepared from a redox reaction between Mn^{2+} and $S_2O_8^{2-}$. α-phase is formed because the presence of Ce^{3+} at 2x2 tunnel prevents structure collapsing. It was found that doping Ce not only induces the phase transformation of MnO_2 but also changes size of nanorod (Figure 2.9). When β-phase is transformed to α-phase, specific capacitance is significantly increased from 13.1 to 57 F g^{-1}. Moreover, the highest specific capacitance is found on the sample which has the smallest size of nanorod compared to the others. The experiment showed that higher specific capacitance was obtained from α-phase (2x2 tunnel) which has larger tunnel size comparing to β-phase (1x1 tunnel), and sample with smaller particle size give more specific capacitance.

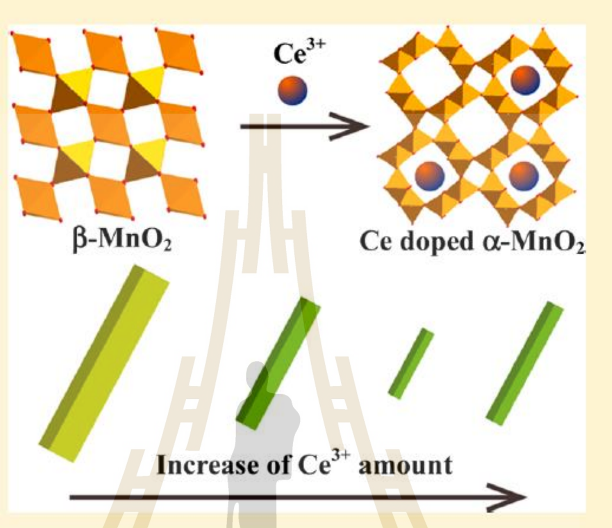

Figure 2.9 Phase transformation of MnO_2 and relation between nanorod size and amount of doped Ce^{3+} (Chen *et al.*, 2016)

Ragupathy *et al.* (2009) studied capacity retention on nanoδ-MnO_2 and also investigated the effects of synthetic condition on its structure. δ-MnO_2 is prepared via direct reaction between $KMnO_4$ and ethylene glycol. The solution was dried at different temperatures to observe structure change and electrochemical behavior. It was found that δ-MnO_2 changed to α-MnO_2 at temperature above 400 ^{o}C. As a result, specific capacitance and specific surface area dramatically decreased when δ-MnO_2 is changed to α-MnO_2. The results obtained from this work indicate that large ion transporting channel of δ-MnO_2 demonstrate more specific capacitance than 1D structure of α-MnO_2 which has narrow tunnel compared to interlayer structure.

Zhang *et al.* (2014) synthesized Na-OL-1 MnO_2 (δ-MnO_2) and Na-OMS-5 MnO_2 (Figure 2.10) and studied their electrochemical performance. The result showed that BET surface area of Na-OL-1 MnO_2 and Na-OMS-5 are 43.9 and 66.8 $m^2\ g^{-1}$. Although, specific surface area of Na-OL-1 is lower than Na-OMS-5, specific capacitance of Na-OL-1 MnO_2 is 308 $F\ g^{-1}$ which is higher than Na-OMS-5 (141 $F\ g^{-1}$) because surface area has limited impact on specific capacitance and the opened 2D structure enhancing cation intercalation into bulk material. Moreover, in this study, not only specific capacitance was studied but the total charge, outer charge and inter charge were also determined as a function of varied scan rate (Table 2.6). The results showed that outer charge is significantly lower than inner charge in both MnO_2 structure which suggests that the intercalation/deintercalation is the main charge storage mechanism compared to adsorption/desorption in Na-OL-1 and Na-OMS-5.

Figure 2.10 Structures of Na-OL-1 (δ-MnO_2) and Na-OMS-5 (Zhang *et al.*, 2014).

Table 2.6 Total charge, outer charge and inner charge of Na-OL-1 and Na-OMS-5.

Type of MnO_2	Total charge ($C\ g^{-1}$)	Outer charge ($C\ g^{-1}$)	Inner charge ($C\ g^{-1}$)
Na-OL-1	1362	85	1277
Na-OMS-5	420	61	359

Devaraj and Munichadraiah (2008) studied the effects of crystallographic structure from five types of MnO_2: α, β, γ, δ and λ on its electrochemical properties. They found that specific capacitance value decreased in the order ofα, δ, γ, λ to β. The presence of large tunnel size in some MnO_2 structure such as α-type (2x2) and δ-type (layered structure) were more suitable for ion insertion and extraction compared to γ-type (1x2) and β-type (1x1) which have narrow channel. MnO_2 with large channel size tends to be good for charge accumulation and have more specific capacitance even though its specific surface area was lower than the others (Table 2.7). As a result, it was concluded that tunnel size plays an important role in the ion insertion and extraction process which significantly affects the specific capacitance.

Table 2.7 Comparison between specific area and capacitance of several types of MnO_2.

Type of MnO_2	Crystal structure	Specific area ($m^2\ g^{-1}$)	Specific capacitance ($F\ g^{-1}$)
α		17.29	241
β	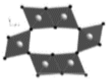	31.56	107
δ	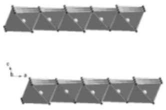	20.93	236
λ	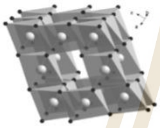	5.21	21

Ghodbane *et al.* (2009) also studied the effects of MnO_2 crystal structure on charge storage properties. Seven types of MnO_2: pyrolusite, ramsdellite, cryptomelane, Ni-todorokite, OMS-5, birnessite and spinel have been investigated. Phase purity, morphology, specific surface area, specific capacitance, electronic and ionic conductivity of MnO_2 were measured. It was found that electronic conductivity of all MnO_2 was not significantly different, but the different channel size resulted in the different ionic conductivity. As their specific capacitances were different despite the similar electronic conductivity, it was concluded that charge storage mechanism of MnO_2 was mainly pseudocapacitance rather than double layer capacitance. The results also showed that ionic conductivity increase with the increasing channel size and connectivity of the structure. Additionally, the presence of Ni^{2+} in Todorokite hiders ion insertion/extraction and decrease both ionic conductivity and specific capacitance which ensures that tunnel size of MnO_2 strongly impacts the capacitance. However, specific surface area is anticipated to play some roles on the specific capacitance of MnO_2 as well. The ionic conductivity, specific surface area and specific capacitance are compared and shown in Figure 2.11. Despite having a relatively small tunnel (1x1), it was found that the three-dimensional interconnected channel in spinel MnO_2 promotion diffusion allowing the high capacitance. In fact, Ghodbane *et al.* (2009) reported that it has the highest capacitance followed by birnessite, OMS-5, cryptomelane, ramsdellite, Ni-todorokite and pyrolusite, respectively.

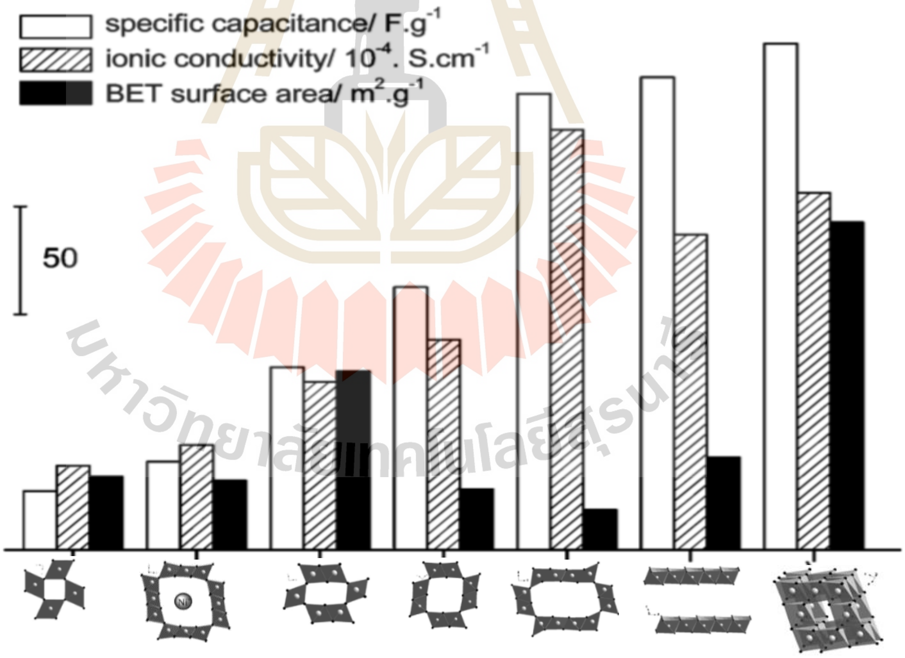

Figure 2.11 Relative values of specific capacitance, ionic conductivity and BET surface area of MnO_2 with different structure (Ghodbane *et al.*, 2009).

According to the investigation of Ghodbane, Pascal and Favier (2009), spinel-MnO_2 is an interesting structure for supercapacitor application due to the high specific capacitance and ionic conductivity.

General formula of spinel oxides is AB_2O_4 with oxide anion arranged in face-centered lattice and cation A and B occupying tetrahedral and octahedral site, respectively (Figure 2.12). Oxidation state of B could be divalent, trivalent and tetravalent and that of A could be monovalent and divalent depending on types of elements. For spinel-MnO_2, Mn occupied octahedral site and its oxidation state is 4+ while the tetrahedral sites are empty. It was first synthesized by acid leaching of $LiMn_2O_4$ (Hunter, 1981).

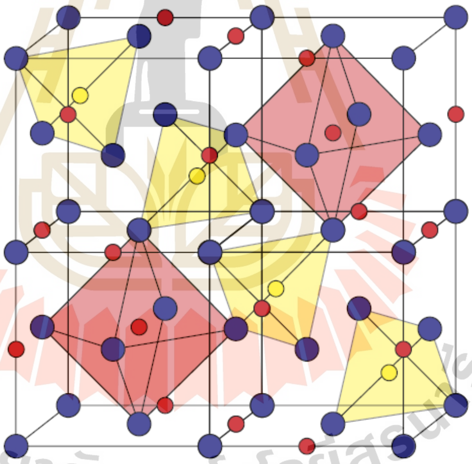

Figure 2.12 Spinel structure: blue spheres represent oxygen while red spheres are B cation and yellow spheres are Acation (Uberuaga *et al.*, 2015).

It was found that structural cavity size ofspinel-MnO_2 is 2.9 Å in radius which is too small for hydrated cation intercalation such as hydrated K^+ and Li^+. Thus, diffusion of cation is achieved only by diffusion of desolvated cation such as K^+ (1.51

Å) and Li^+ (0.73 Å) into tetrahedral sites whose radius is about 1.94 Å (Ghodbane *et al.*, 2012).

Increasing of d-spacing and lattice parameters have a possibility in increasing cavity size of tetrahedral site which would allow more ion diffusion. One way to increase the cell is to dope larger elements in manganese site. Many metals such as Sc, Cr, Co, Ni, Zn, In, Ge, Fe and Ti have been doped in $LiMn_2O_4$, but most resulted in similar lattice parameters (Xie *et al.*, 2005; Wu *et al.*, 2002; Guler *et al.*, 2014). Only Ge, Fe and Ti doping increase cell parameters (Tarascon *et al.*, 1991). Among these compounds, acid leached Ti-doped $LiMn_2O_4$ had the largest cell parameter (Table 2.8) and is the focus of this current research.

Table 2.8 Cell parameters of acid leached $LiMn_{2-x}M_xO_4$ when x = Ti, Ge and Fe (Tarascon *et al.*, 1991).

Compounds	Cell parameter (Å)
Leached $LiTiMnO_4$	8.153
Leached $LiGe_{0.2}Mn_{1.8}O4$	8.052
Leached $LiFe_{0.2}Mn_{1.8}O_4$	8.082
Leached $LiMn_2O_4$	8.022

2.4 Research objectives

1. To prepare Ti doped MnO_2 with spinel structure.

2. To study the structure, physical and electrochemical properties of the obtained materials.

3. To explain the effects of structure and composition on properties of the obtained compounds.

CHAPTER III

EXPERIMENTAL

3.1 Chemicals and materials

- Lithium carbonate (Li_2CO_3), 99%, Acros Organic
- Manganese (II) acetate tetrahydrate ($Mn(CH_3COO)_2 \cdot 4H_2O$), 99%, Acros Organic
- Titanium dioxide (TiO_2), 99%, Sigma-Aldrich
- Hydrochloric acid (HCl), 37%, Carlo Erba
- Polyvinylidine fluoride (PVDF), 99%, Acros Organic
- N-methyl-2-pyrrolidone ($CH_3NCOC_2H_6$), 99%, Acros Organic
- Acetone (CH_3COCH_3), 99.8%, Carlo Erba
- Potassium sulfate (K_2SO_4), 99%, Carlo Erba
- Carbon black, 99%, Sigma-Aldrich
- Nickel foam (1x0.5 cm^2), Sigma-Aldrich

3.2 Instruments

- Powder X-Ray diffractometer (XRD), Bruker D2 Phaser
- Scanning electron microscope coupled with energy dispersive spectroscope (SEM-EDS), JSM-6010 LV, JEOL

- Inductively coupled plasma optical emission spectrometer (ICP-OES), optima8000, PerkinElmer
- X-ray absorption spectroscope, beam line 5.2, Synchrotron Light Research Institute
- Potentiostate, Reference 600, Gamry instrument
- BET surface area analyzer, Bel sorp Mini II

3.3 Sample preparation

3.3.1 Solid state method

Solid state method is a classic process used for solid synthesis. Solid state synthesis has been widely used because it is simple, solventless and reagentless. In a typical method, solid state precursors were mixed together in a mortar and finely ground and mixed by a pestle. Highly volatile organic solvents such as acetone and ethanol were used to improve sample homogeneity in the grinding process. After that, the mixture was heated under designated condition to obtain the product.

In this work, stoichiometric mixtures of lithium carbonate, manganese acetate tetra hydrate and titanium dioxide were mixed with 5 mL of acetone and crushed in a mortar with a pestle. The mixtures were first calcined at 350 ^{o}C for 12 hours to eliminate acetate. After that, the mixtures were finely ground, pressed into pellets and sintered at 800 ^{o}C for 12 hours 2 times to give products.

3.3.2 Acid leaching for lithium extraction

Strong acidic solution is a common reagent used for lithium extraction from lithium metal compounds such as $LiCoO_2$ and $LiMn_2O_4$ to produce metal oxide residues.

According to equation (3.1) (Hunter, 1981), extraction of lithium takes place by disproportionation of Mn^{3+} to Mn^{4+} and Mn^{2+} when the compound reacts with diluted HCl solution. As a result, MnO_2 is obtained as the only non-soluble product.

$$2LiMn_2O_4 + 4HCl \longrightarrow 2LiCl + 3MnO_2 + MnCl_2 + 2H_2O \qquad (3.1)$$

To prepare leached $LiMn_{2-x}Ti_xO_4$, the solid products of $LiTi_xMn_{2-x}O_4$ obtained from solid state reaction were dispersed in 0.5 M HCl solution and stirred for 48 hours at room temperature. After that, the resulting suspension was filtered by cellulose acetate filter paper (0.45 micron diameter) and the non-soluble residues were collected.

3.3.3 Preparation of electrodes

Electrodes are composed of 80 weight% of the samples, 10 weightt% of acetylene black and 10 wt % of polyvinylidene fluoride as a binder. All components were mixed and crushed with 5 mL of acetone. After all acetone is evaporated, the resulting powder was mixed with 5 mL of N-methyl-2-pyrrolidone by sonification for 3 minutes. The resulting black suspension was coated onto Ni foam by dropping with micropipette, and subsequently dried at 100 ^{o}C in an oven. A step of coating and drying was repeated to get loading mass close to 0.5 mg cm^{-2}. Finally, the electrodes were dried at 130 ^{o}C overnight and immerged in 0.5 M K_2SO_4 solution prior to electrochemical characterization.

3.4 Characterizations

3.4.1 Structural and physical characterization

3.4.1.1 Powder X-ray diffraction (XRD)

In this study, the X-ray powder diffraction patterns were used as a fingerprint of samples for phase identification and phase purity confirmation.

$LiMn_{2-x}Ti_xO_4$ and leached $LiMn_{2-x}Ti_xO_4$ powders were investigated by powder X-ray diffraction technique (XRD) using Bruker D2 Phaser diffractometer (Cu Kα radiation) in Bragg-Brentano configuration. Short step-scan data for phase identification were recorded in the angle interval 10–60 (2θ) with a step of 0.02^o (2θ) and a counting time of 0.2 second per step, and long step-scan data were in the angle interval $10–120^o$ (2θ) with a step of 0.02^o (2θ) and a counting time of 2 second per step. Lattice parameters, unit cell volume, crystallographic information including atomic position and occupancies were determined by Reitveld refinement using a TOPAS software. In a typical refinement, the occupancy of oxygen was fixed while those of other elements were refined. The total occupancies of Li, Mn, and Ti in leached $LiMn_{2-x}TixO_4$ were fixed to the values obtained from chemical analyses.

3.4.1.2 Scanning electron microscopy (SEM) and energy-dispersive X-ray spectroscopy (EDS)

In this study, SEM provides morphology, particle size, shape, and distribution of sample particles. In the experiment, the samples were coated with a layer of gold using a Balzer sputtering coater and characterized with a scanning electron microscope, (SEM-EDS), JSM-6010 LV, JEOL. EDS (SEM-EDS), JSM-6010 LV, JEOL is used for elemental analysis in this study.

3.4.1.3 Inductively coupled plasma optical emission spectrometry (ICP-OES)

In this study, ICP-OES optima8000, PerkinElmer was used to determine the amount of Li, Mn and Ti in the solution obtained from acid leaching of $LiMn_{2-x}Ti_xO_4$ by calibration curve quantification. Standard solution of lithium, manganese and titanium were prepared from lithium acetate, manganese acetate and ammonium hexafluorotitanate.

3.4.1.4 X-ray absorption spectroscopy (XAS)

Oxidation state of Mn and Ti in the solid products was investigated by X-ray absorption spectroscopy (XAS). The measurements of Mn K-edge and Ti K-edge XANES spectra were carried out in transmission mode at beam line BL-5.2 in Synchrotron light research institute (SLRI), Nakonrachasrima. MnO, Mn_2O_3 and MnO_2 were used as standard for Mn^{2+}, Mn^{3+} and Mn^{4+}, respectively. Ti_2O_3 and TiO_2 (rutile) were used as standard for Ti^{3+} and Ti^{4+}, respectively. XAS measurement was performed under Ar atmosphere at room temperature.

3.4.1.5 Gas adsorption

In this study, BET measurement was used to investigate the specific area and pore volume of the obtained materials. Samples were weighted and put in a tube. Each sample was degassed at 200 ^{o}C for 4 hours under vacuum to remove moisture. N_2 gas was slowly filled in the tube. The specific surface area of the sample was calculated following the Brunner Emmet Teller (BET) method and the Barrett Joyner Halenda (BJH) method at the relative pressure range 0 - 1 (p/p_0) of liquid nitrogen and the total volume was calculated from a single point at p/p_0 ~1. Data were analyzed using the Brunner-Emmett-Teller (BET), Barrett-Joyner-Halenda (BJH), and t-plot methods.

3.4.2 Electrochemical characterization

Cyclic voltammetry is an electrochemical measurement using electrochemical cell which consists of 3 conventional electrodes: a working electrode, a counter electrode and a reference electrode. When the potential window is set, working electrode potential is linearly ramped. After the potential reached the set point, the potential is ramped in the opposite direction returning to the initial value. Voltammogram showing electrochemical characteristic information of materials is a plot of current counted by the working electrode versus the applied potential.

Specific capacitance (C_s) can be calculated by equation (3.2) and (3.3) where Q is collected charge in coulomb, ΔV is potential window, m is material mass in gram, v is scan rate ($v\ s^{-1}$) and I is current in ampere.

$$C_s = Q/\Delta Vm \tag{3.2}$$

$$C_s = \int IdV/v\Delta Vm \tag{3.3}$$

In this work, three conventional electrodes composing of Pt counter electrode, Ag/AgCl reference electrode and a composite electrode as a working electrode were used. 0.5 M K_2SO_4 solution was used as an electrolyte. Potential window was set in the range of 0.9 V to -0.1 V. The potential step was set to 0.5 mV.

CHAPTER IV

RESULTS AND DISCUSSIONS

4.1 Structure and phase purity analysis

4.1.1 X-ray diffraction

Figure 4.1 shows XRD patterns of $LiMn_{2-x}Ti_xO_4$ and leached $LiMn_{2-x}Ti_xO_4$ in 2θ range of 10° to 60°. Diffraction peaks of both series can be indexed to cubic spinel structure with $Fd\bar{3}m$ space group, in accordance with previous reports (Tarascon *et al.*, 1991; Wang *et al.*, 2014; Ma *et al.*, 2010; Krins *et al.*, 2006; Zhang *et al.*, 2015). No impurity phase arises with the increase of Ti content until $x = 0.75$. Impurity is observed in a sample with $x = 1$ (Figure 4.2) showing that solubility limit of Ti in $LiMn_{2-x}Ti_xO_4$ is 0.75. Mn and Ti are supposed to be in 16d site and Li is located in 8a site due to their ionic radius. However, previous studies (Avdeev *et al.*, 2009; Petrov *et al.*, 2005; Vu *et al.*, 2017) reported that Ti and Mn are able to replace some Li in 8a site which can be observed by the increase of (220) diffraction when x is increased (Wang *et al.*, 2014). This increase of (220) intensity is also observed in this work as shown in Figure 4.2. However, different synthetic route and sintering temperature also affect occupancies of Ti and Mn. It was found that samples prepared by quenching and sintering at 1000 °C have more Mn/Ti in 8a site. Thus, (220) peak intensity is higher comparing to that of the samples prepared at 800 °C without quenching (Petrov *et al.*, 2005; Vu *et al.*, 2017). After deintercalaction process, 8a site is almost vacant.

Thus, the (220) plane is not observed in leached $LiMn_{2-x}Ti_xO_4$. In addition, XRD patterns of leached $LiMn_{2-x}Ti_xO_4$ shows that peak intensity of (400) plane is increased with the amount of Ti (Figure 4.3) which agrees with that reported by Avdeev *et al.* (2009). The XRD peaks continuously shift toward lower diffraction angles when x is increased in both series confirming the expansion of lattice parameter. Figure 4.4 shows the lattice parameter change in both $LiMn_{2-x}Ti_xO_4$ and leached $LiMn_{2-x}Ti_xO_4$. In this case, lattice parameters of all samples trend to increase when doping content is increased because the ionic radii of Ti^{4+} ion (0.605 Å) is larger than that of Mn^{4+} ions (0.530 Å) which also indicating that Ti ions are successfully doped into the Mn position in spinel structure (Shannon and Prewitt, 1969; Shannon, 1976; Scordari,1992). On the other hand, lattice parameters of leached $LiMn_{2-x}Ti_xO_4$ are smaller than those of $LiMn_{2-x}Ti_xO_4$ due to the extraction of Li and the oxidation of Mn^{3+} to Mn^{4+} after acid leaching process as ionic radii of Mn^{4+} is smaller than that of Mn^{3+} (0.645 Å).

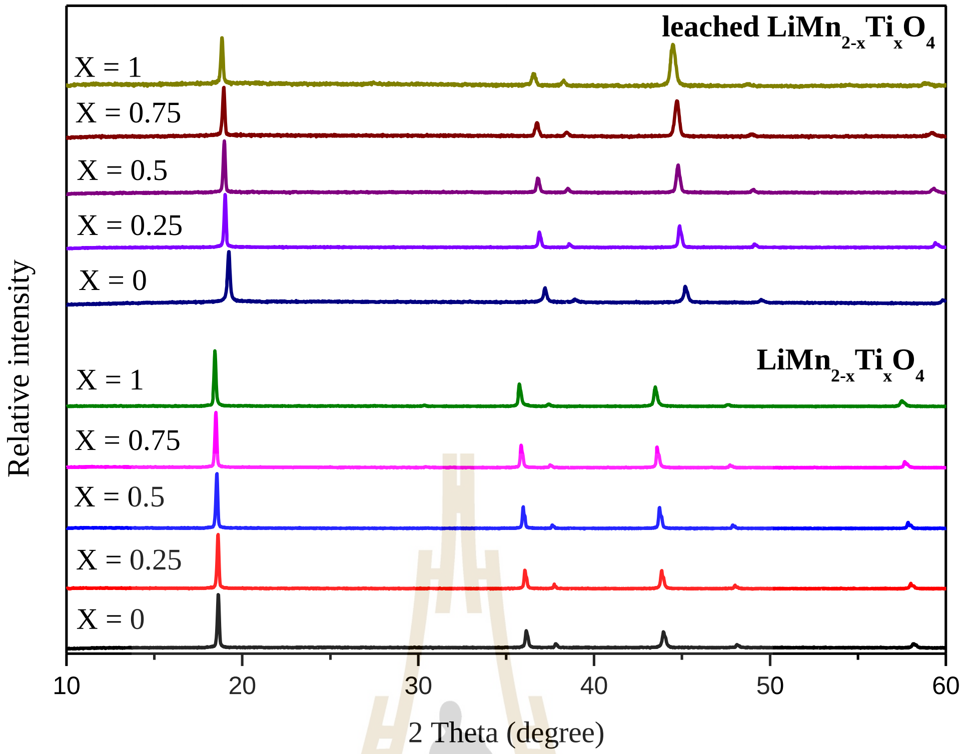

Figure 4.1 XRD patterns of $LiMn_{2-x}Ti_xO_4$ and leached $LiMn_{2-x}Ti_xO_4$.

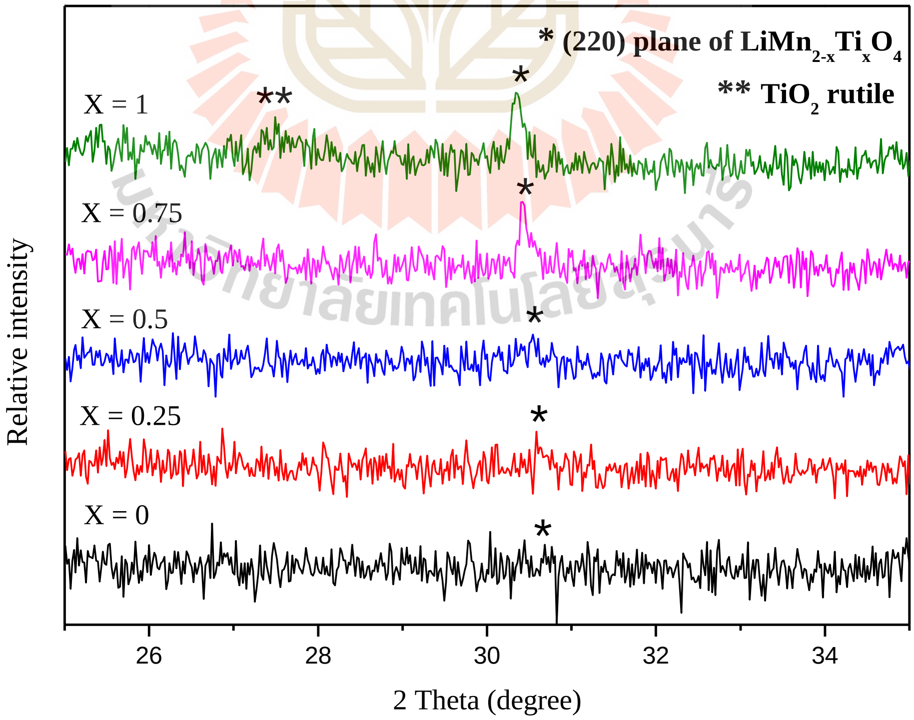

Figure 4.2 Close-up XRD patterns of $LiMn_{2-x}Ti_xO_4$.

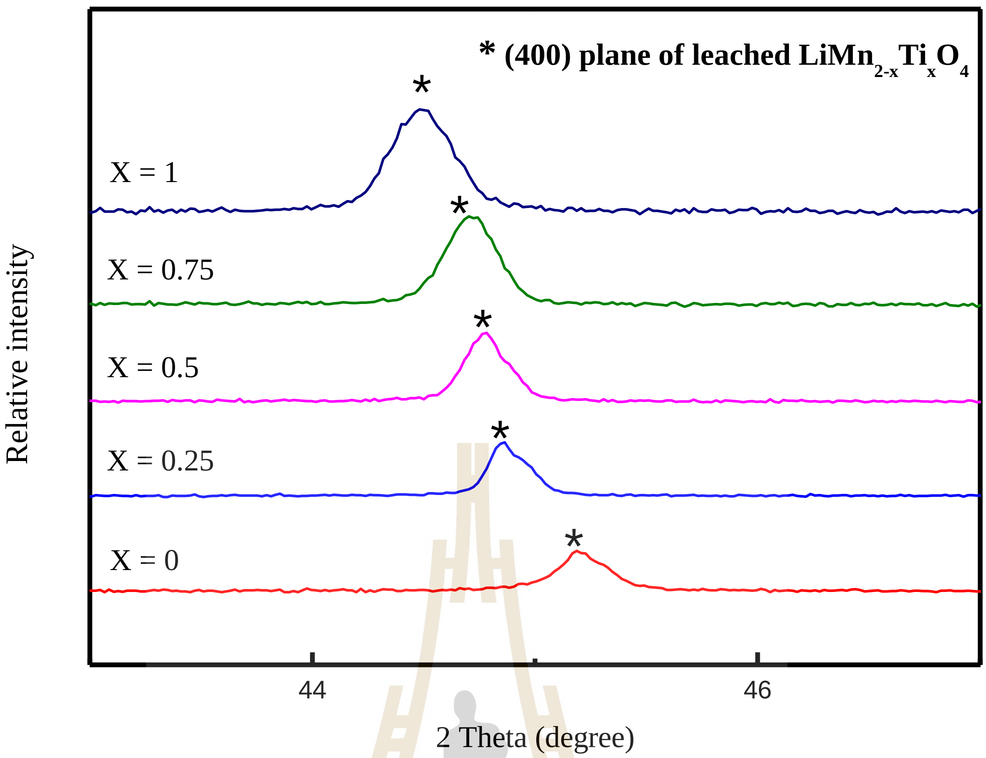

Figure 4.3 Close-up XRD patterns of leached $LiMn_{2-x}Ti_xO_4$.

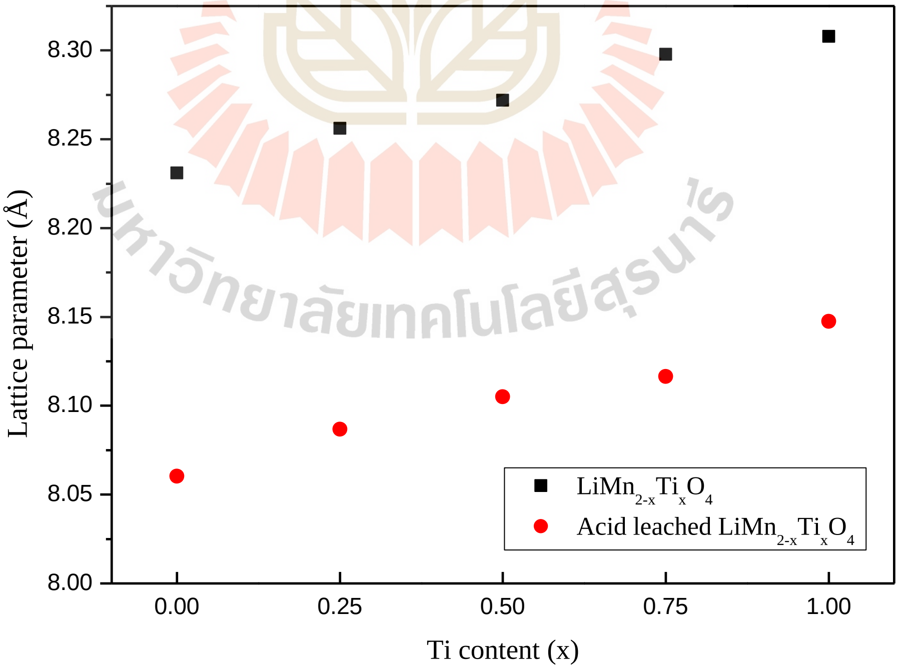

Figure 4.4 Lattice parameters of $LiMn_{2-x}Ti_xO_4$ and leached $LiMn_{2-x}Ti_xO_4$ series.

4.1.2 Rietveld refinement

Rietveld refinement was performed to study site and occupancy of Ti and Mn in the leached $LiMn_{2-x}Ti_xO_4$. Spinel structure and site occupation are shown in Figure 4.5. Refined parameters for leached $LiMn_{2-x}Ti_xO_4$ when x = 0, 0.25, 0.5 and 0.75 are shown in Table 4.1. However, the sample with x = 1 was not refined because the presence of TiO_2 impurity could provide inaccurate determination of cation occupancies in each position. The refinement data show that 8a site is almost vacant as Li^+ are leached, and 16d site is mainly occupied by Mn^{4+} and Ti^{4+}. Although, almost all Li^+ are extracted from 8a site, a small amount of Li^+ is still present and trapped in 16d site (Avdeev *et al*., 2009). Moreover, it was found that Ti^{4+} occupies in 8a site. Occupancy of Ti^{4+} in 8a slightly increases when Ti content in leached $LiMn_{2-x}Ti_xO_4$ is increased. Interestingly, the data also shows that Mn^{3+} occupies 16c site. It was found that occupancy of Mn^{3+} in 16c increases when Ti content is increased (Figure 4.6). The occupancy of Mn^{3+} in 16c site is explained by site preference and electron hopping process. The Li extraction is achieved by disproportionation of Mn^{3+} in 16d site and oxidation of Mn^{2+} in 8a site. In the case of Mn^{2+}, electrons move from bulk Mn^{2+} to Mn^{4+}, and both ions transform to Mn^{3+}. However, the octahedral site preference of Mn^{3+} is very high (Avdeev *et al*., 2009). Therefore, Mn^{3+} should shift from 8a site to the adjacent 16c site which has lower energy site preference.

Table 4.1 Refined parameters and reliability factor for leached $LiMn_{2-x}Ti_2O_4$.

Atom	Site	Occupancy	Beq
X = 0; 8.0603(24) Å, Rexp : 1.50 Rwp : 2.90 GOF : 1.94			
Mn	16d (0.5, 0.5, 0.5)	1.00(1)	0.5
O^{2-}	32e (u,u,u), u = 0.2665(3)	1	1.0
X = 0.25; 8.0867(1) Å, Rexp : 1.29 Rwp : 2.29 GOF : 1.78			
Li^{+}	16d (0.5, 0.5, 0.5)	0.054(2)	0.5
Li^{+}	8a (0.125, 0.125, 0.125)	0.073(5)	0.5
Mn^{3+}	16c (0, 0, 0)	0.039(1)	0.5
Mn^{3+}	16d (0.5, 0.5, 0.5)	0.051(11)	0.5
Mn^{4+}	16d (0.5, 0.5, 0.5)	0.78	0.5
Ti^{4+}	16d (0.5, 0.5, 0.5)	0.116(2)	0.5
Ti^{4+}	8a (0.125, 0.125, 0.125)	0.018(4)	0.5
O^{2-}	32e (u,u,u), u = 0.2610(2)	1	1.0

Table 4.1 Refined parameters and reliability factor for leached $LiMn_{2-x}Ti_2O_4$ (Continued).

Atom	Site	Occupancy	Beq
X = 0.5; 8.1050(1) Å, Rexp : 1.42 Rwp : 2.50 GOF : 1.75			
Li^+	16d (0.5, 0.5, 0.5)	0.06	0.5
Mn^{3+}	16c (0, 0, 0)	0.06	0.5
Mn^{4+}	16c (0, 0, 0)	0.040(1)	0.5
Mn^{4+}	16d (0.5, 0.5, 0.5)	0.630(1)	0.5
Ti	16d (0.5, 0.5, 0.5)	0.234(2)	0.5
Ti	8a (0.125, 0.125, 0.125)	0.032(3)	0.5
O	32e (u,u,u), u = 0. 2583(2)	1	1.0

Table 4.1 Refined parameters and reliability factor for leached $LiMn_{2-x}Ti_2O_4$ (Continued).

Atom	Site	Occupancy	Beq
X = 0.75; 8.1165(2) Å, Rexp : 1.60 Rwp : 2.80 GOF : 1.75			
Li^+	16d (0.5, 0.5, 0.5)	0.045	0.5
Mn^{3+}	16c (0, 0, 0)	0.045	0.5
Mn^{4+}	16c (0, 0, 0)	0.116(1)	0.5
Mn^{4+}	16d (0.5, 0.5, 0.5)	0.434(1)	0.5
Ti^{4+}	16d (0.5, 0.5, 0.5)	0.367(2)	0.5
Ti^{4+}	8a (0.125, 0.125, 0.125)	0.017(4)	0.5
O^{2-}	32e (u,u,u), u = 0.2572(2)	1	1.0

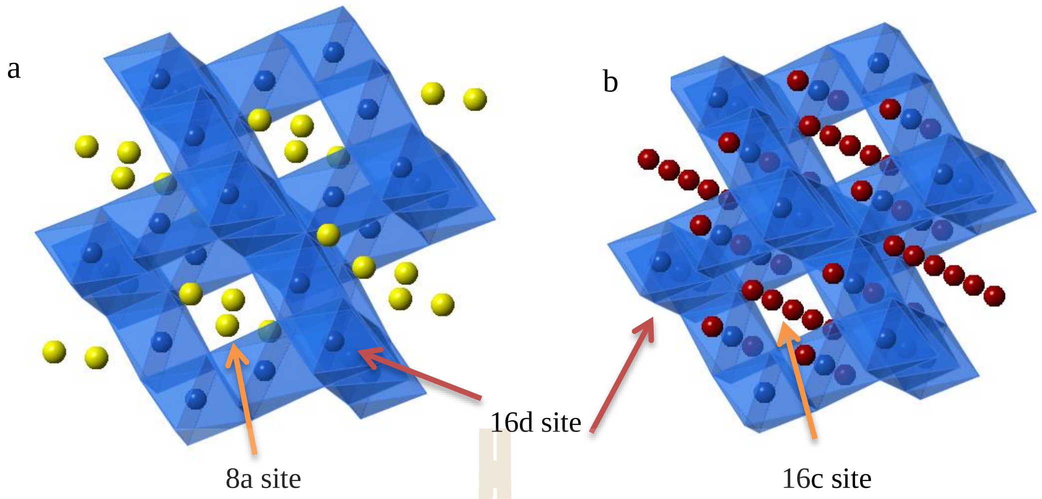

Figure 4.5 Spinel structure and site occupation.

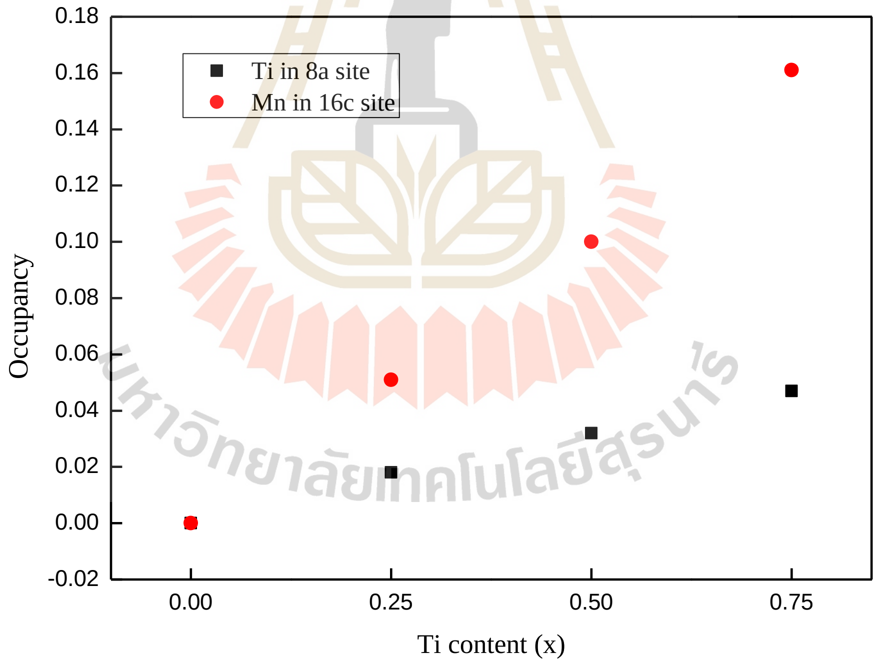

Figure 4.6 Occupancy of Ti in 8a site and Mn in 16d site in leached LiMn$_{2-x}$Ti$_x$O$_4$.

4.2 Oxidation state and elemental analysis

4.2.1 X-ray absorption spectroscopy

Figure 4.7 and 4.8 show the Ti K-edge and Mn K-edge XANES spectra for each sample at room temperature. K-edge XANES spectra of Ti in $LiMn_{2-x}Ti_xO_4$ and leached $LiMn_{2-x}Ti_xO_4$ are shown in Figure 4.7. Pre-edge indicates 1s electron into hybridized Ti 3d/4p states with e_g symmetry. Its intensity is influence by the coordination of Ti. Apparently, pre-edge intensity of leached samples is higher than that of pre-leached samples suggesting that not only Ti located in octahedral site (16d site) but it also occupies tetrahedral site (8a site) when Li is removed. The higher intensity of Ti pre-edge in the leached products indicates that amount of Ti in 8a site is higher in leached sample comparing to pre-leached samples. In addition, Ti spectra lie between spectrum of Ti_2O_3 and TiO_2 (rutile phase). Although the energy edge position could imply that Ti is in mixed valence state between 3+ and 4+, it is unlikely. There is no report about Ti^{3+} in spinel $LiMn_{2-x}Ti_xO_4$. On the other hand, few studies on oxidation state of Ti in $LiMn_{2-x}Ti_xO_4$ indicate only Ti^{4+} (Murphy *et al*., 2015). In addition, it was found that Ti^{4+} in different structure has different K-edge energy (Balzarotti, 1980). Thus, it is concluded that oxidation state of Ti is 4+ in both $LiMn_{2-x}Ti_xO_4$ and leached $LiMn_{2-x}Ti_xO_4$ and the slight shift in the edge energy is due to the change in crystallographic structure.

K-edge XANES spectra of Mn in $LiMn_{2-x}Ti_xO_4$ and leached $LiMn_{2-x}Ti_xO_4$ are shown in Figure 4.8. The pre-edge arises from dipole-forbidden 1s to 3p transition of Mn. Pre-edge intensity could be used to indicate coordination of Mn. In both $LiMn_{2-x}Ti_xO_4$ and leached $LiMn_{2-x}Ti_xO_4$, the pre-edge intensity and feature of Mn spectra are not significantly different suggesting the same coordination of Mn.

Moreover, it was found that spectra of Mn K-edge of all samples lie between those of Mn_2O_3 and MnO_2. Edge feature of Mn $LiMn_{2-x}Ti_xO_4$ and leached $LiMn_{2-x}Ti_xO_4$ arise from dipole allowed transition of 1s to 4p (Murphy *et al.*, 2015). The edge position slightly shift to lower energy when x is increased indicating the mixed state of Mn^{3+} and Mn^{4+} in $LiMn_{2-x}Ti_xO_4$ series. Positions of the edge energy also suggest the raising of Mn^{3+} when x is increased. After acid treatment, it was found that spectra of leached $LiMn_{2-x}Ti_xO_4$ overlap with that of standard MnO_2. The results indicate that oxidation state of Mn is changed after acid treatment from mixed valence to 4+ due to oxidation and disproportionation process of Mn.

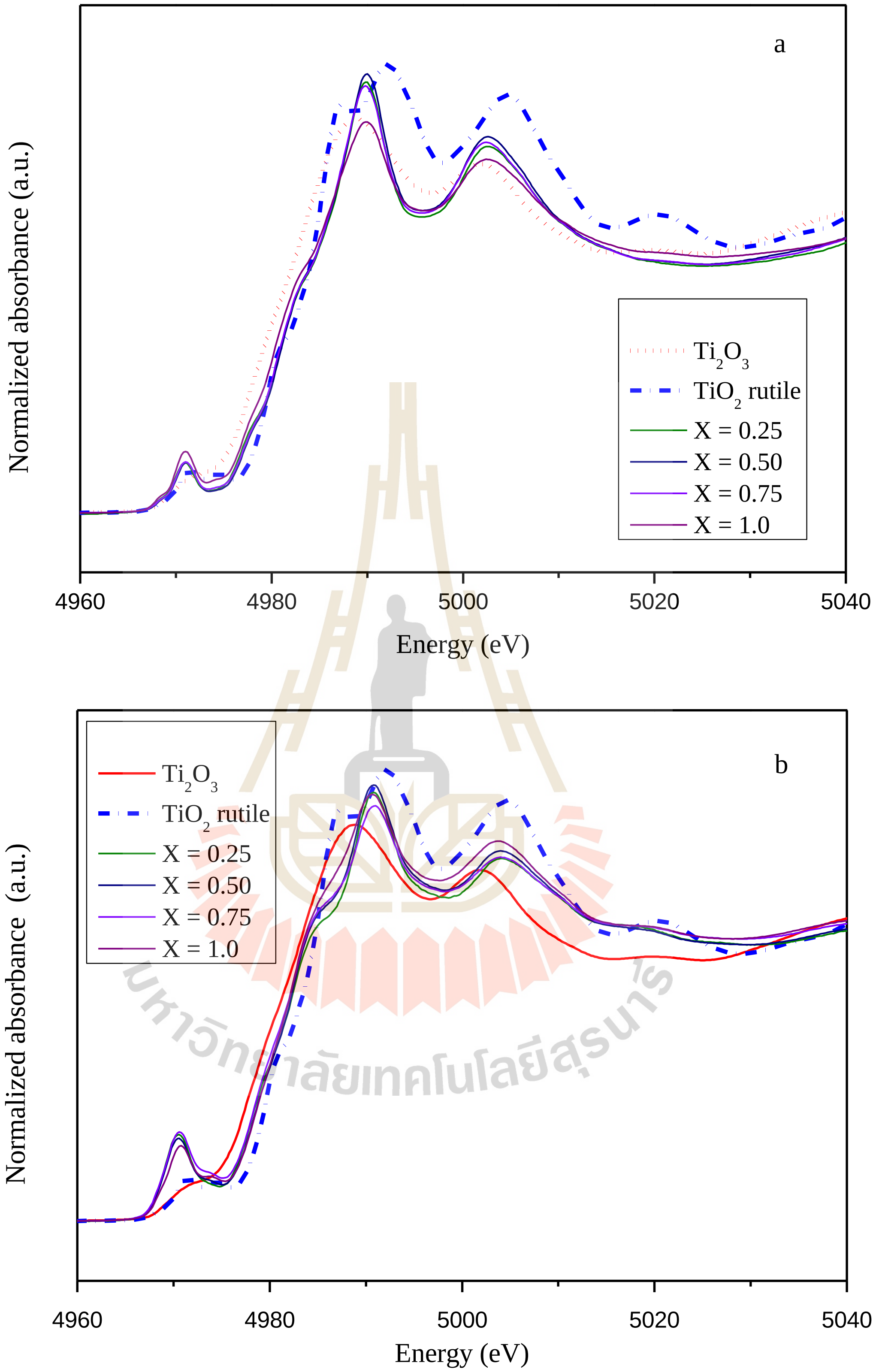

Figure 4.7 Ti K-edge spectra of $LiMn_{2-x}Ti_xO_4$ (a) and leached $LiMn_{2-x}Ti_xO_4$ (b).

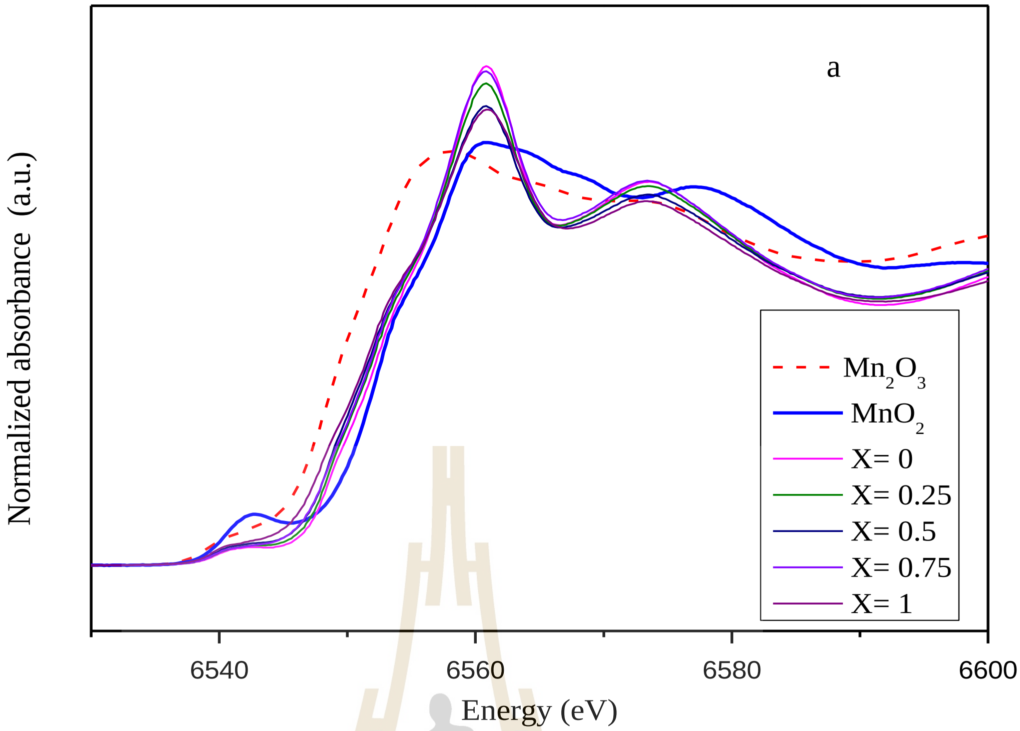

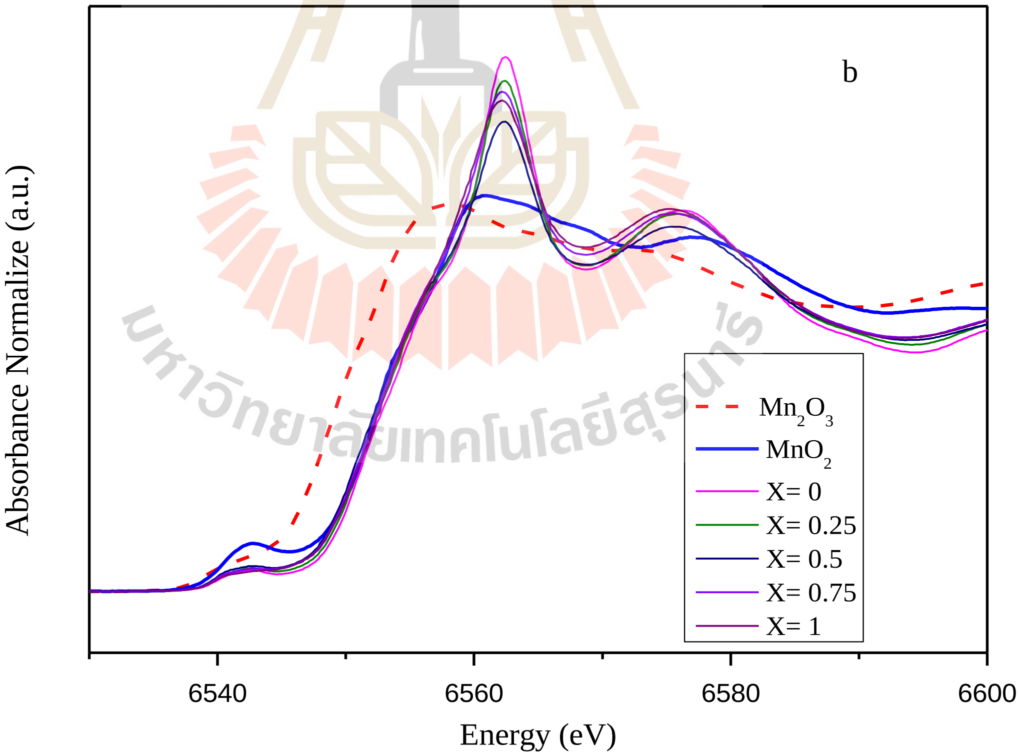

Figure 4.8 Mn K-edge spectra of $LiMn_{2-x}Ti_xO_4$ (a) and leached $LiMn_{2-x}Ti_xO_4$ (b).

4.2.2 Inductively coupled plasma optical emission spectroscopy

To study the elemental ratio of each sample, the amount of Li, Mn and Ti in the leached solution was investigated by ICP-OES. Acid leaching process of $LiTi_xMn_{2-x}O_4$ when x = 0 could be explained by equation (4.1) based on disproportionation reaction of Mn^{3+} (Hunter *et al.*, 1981; Devaraj *et al.*, 2008). However, it was found in some cases that Mn^{3+} cannot completely react with acid, and some of Li is maintained to balance the charge (Ghodbane *et al.*, 2009).

$$2LiMn_2O_4 \longrightarrow 2Li^+ + Mn^{2+} + 3MnO_2 \qquad (4.1)$$

Acid leaching of $LiTi_xMn_{2-x}O_4$ has been studied by Tarascon *et al.* (1991). The equation is more complicated than pristine $LiMn_2O_4$. Ti^{4+} is involved in the reaction as described by equation (4.2).

$$2(2-y)LiTi_xMn_{2-x}O_4 + 4(2-y)H^+ \longrightarrow (2-y)Mn^{2+} + yTiO_2 + 2(2-y)Li^+ + 2(2-y)H_2O + (3-2y)Ti_xMn_{2-x}O_4 \qquad (4.2)$$

According to equation (4.2), not only that Mn^{2+} and Li^+ were extracted from the sample, but Ti^{4+} was also removed from $LiTi_xMn_{2-x}O_4$. To determine the product empirical formula, Li, Mn and Ti ion in the leached solution were determined by ICP-OES. The final formula of residual product was calculated from the elemental difference between $LiTi_xMn_{2-x}O_4$ and ions in the solution. As shown in Table 4.2, it was found that elemental composition of the leached samples are similar to those of $LiTi_xMn_{2-x}O_4$ which agree well with equation (4.2). However, complete removal of Li cannot be achieved when Ti content is increased. Two different explanations were given for the incomplete Li extraction. Tarascon *et al.* (1991) stated that TiO_2 occurred during the reaction covers the particles and blocks the Li removal. On the other hand, Avdeev *et al.* (2009) suggested that complete removal of Li cannot be achieved because only

Li in 8a position could be removed with this method. Thus, Li^+ that occupies 16d position will remain in the solid residues. As summarized in Table 4.2, our leached solution contains Ti which indicates that most TiO_2, if not all, formed during the leaching should be dispersed in the solution and should not significantly hinder the Li removal. On the other hand, the correlation between Li^+ in 8a position and Li^+ in the leached solution is not as clear as reported in the work of Avdeev *et al.* Thus, further analyses are required to clarify this matter.

4.2.3 Energy dispersive x-ray spectroscopy

Although the elemental compositions of all samples were determined from ICP-OES, it is considered an indirect method as the compositions of the leached samples were not directly analyzed. Therefore, energy dispersive X-ray spectroscopy was used to determine the composition of the residual product (Table 4.2). The sample formula obtained after acid treatment was calculated from atomic % of Mn and Ti in solid residual product. Because of the limitation of EDS techniques in analyzing light atoms, only the ratio of Mn and Ti are investigated here. Generally, the EDS results agree well with the ICP-OES.

Table 4.2 Elemental compositions of the samples.

Ti content	Unleached sample (from ICP-OES)	Leached sample	
		ICP-OES	EDS
0	$LiMn_2O_4$	MnO_2	-
0.25	$LiMn_{1.75}Ti_{0.25}O_4$	$Li_{0.18}Mn_{1.74}Ti_{0.25}O_4$	$Li_{1-y}Mn_{1.95}Ti_{0.25}O_4$
0.5	$LiMn_{1.5}Ti_{0.5}O_4$	$Li_{0.12}Mn_{1.46}Ti_{0.5}O_4$	$Li_{1-y}Mn_{1.58}Ti_{0.5}O_4$
0.75	$LiMn_{1.25}Ti_{0.75}O_4$	$Li_{0.09}Mn_{1.19}Ti_{0.75}O_4$	$Li_{1-y}Mn_{1.27}Ti_{0.75}O_4$
1	$LiMnTiO_4$	$Li_{0.1}Mn_{0.89}TiO_4$	$Li_{1-y}Mn_{0.93}TiO_4$

4.3 Surface and morphology

4.3.1 Scanning electron microscopy

SEM images of $LiMn_{2-x}T_{ix}O_4$ and leached $LiMn_{2-x}Ti_xO_4$ (Figure 4.9 and 4.10) provide the morphology and particle size information. The results indicate that particle size is in the range of 1-5 µm. The large particles were formed by aggregation of numerous smaller particles. The morphology of the compounds strongly depended on sample preparation (Ghodbane *et al*., 2009). The results indicate that particle size and shape of all samples synthesized by solid state method are not significantly different and also confirme that leaching process and the increasing of Ti contents do not affect sample morphology and particle size. Moreover, shape and particle size of $LiMn_2O_4$ synthesized by solid state method is similar to those obtained from sol-gel preparation (Wang, Lai *et al*., 2015; Wang, Chen *et al*., 2015).

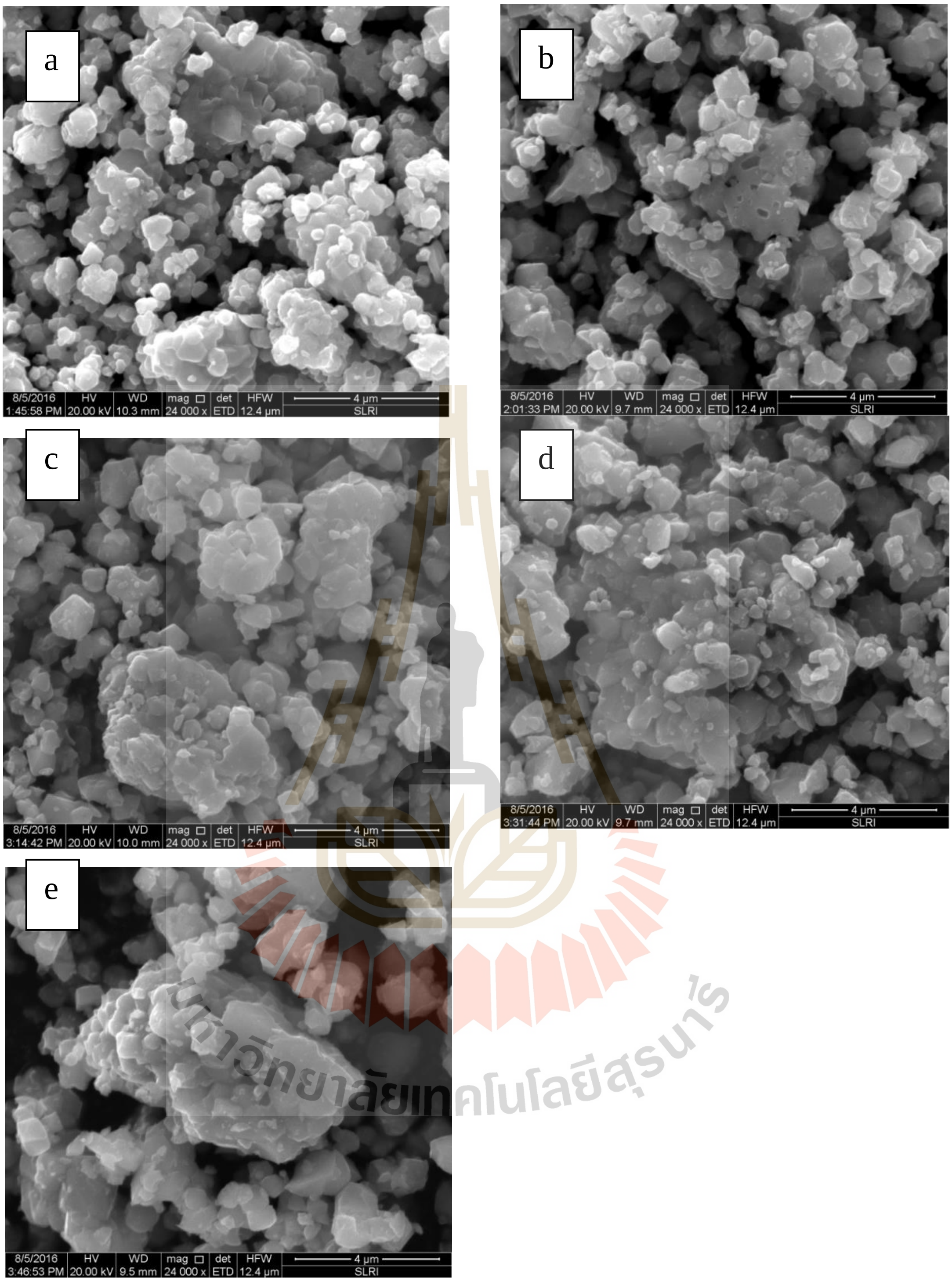

Figure 4.9 SEM images of $LiMn_{2-x}Ti_xO_4$, x=0 (a), x=0.25 (b), x=0.5 (c), x=0.75 (d) and x= 1 (e).

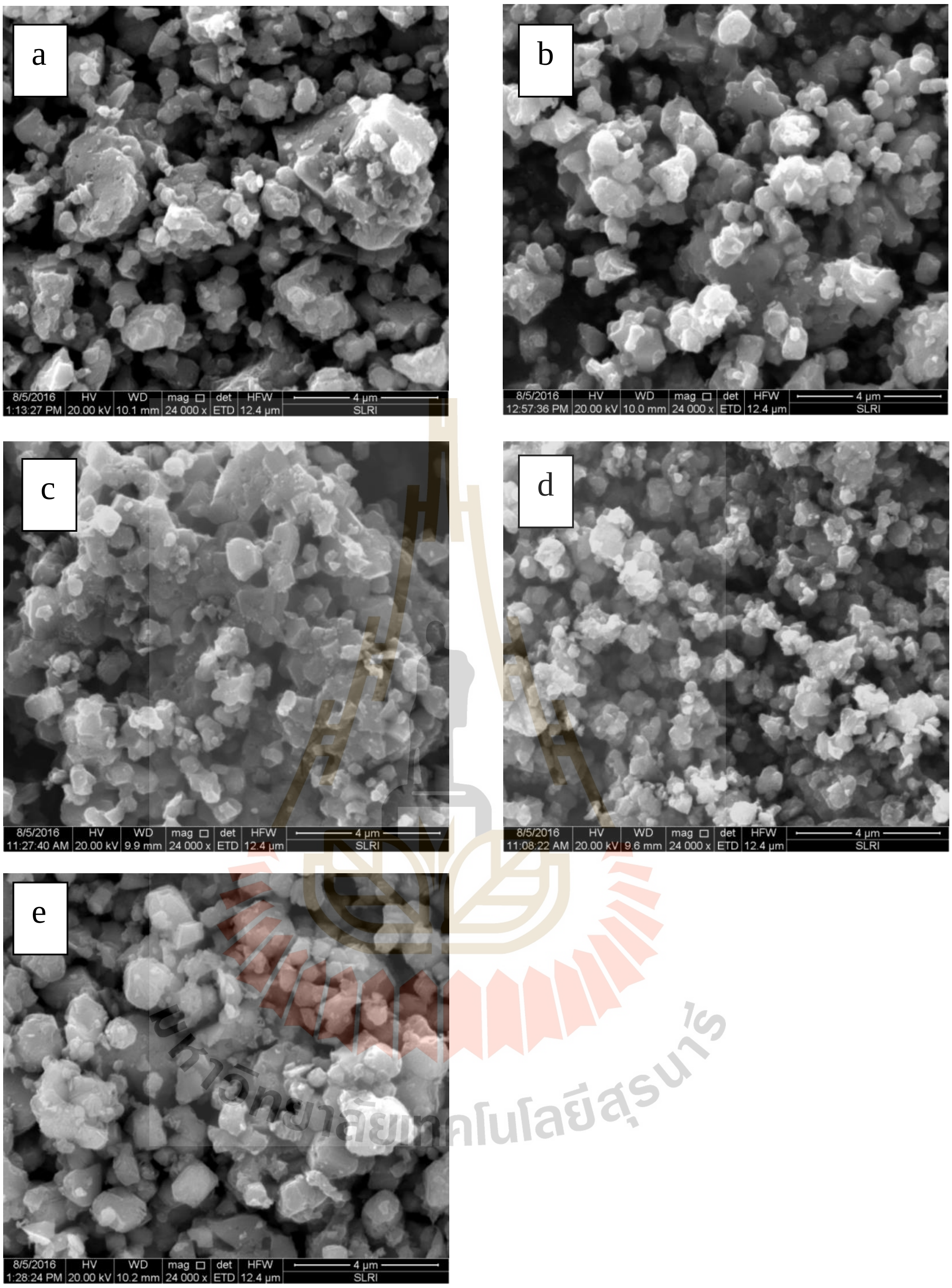

Figure 4.10 SEM images of leached $LiMn_{2-x}Ti_xO_4$, x = 0 (a), x = 0.25 (b), x = 0.5 (c), x = 0.75 (d) and x = 1 (e).

4.3.2 Gas adsorption and BET method

Table 4.3 shows average specific surface area, pore volume and pore diameter. The results indicate that those parameters of all leached $LiMn_{2-x}Ti_xO_4$ samples are not significantly different compared to each other as they were prepared by method. According to the results, specific surface area is related to pore volume. The specific surface area of spinel MnO_2 prepared in this work is similar to that reported by Devaraj *et al.* (2008).

Table 4.3 Average BET surface area of leached $LiMn_{2-x}Ti_xO_4$.

Criteria	x = 0	x = 0.25	x = 0.5	x = 0.75	x = 1
Average **BET** **(m^2 g^{-1})**	17	8	10	9	14
Average total pore volume (cm^3 g^{-1})	0.0665	0.0325	0.046	0.0342	0.069
Average pore diameter (nm)	15.57	15.675	18.99	15.365	19.475

4.4 Electrochemical study

To study the effects of Ti on electrochemical behavior of leached $LiMn_{2-x}Ti_xO_4$, cyclic voltammetry was performed on the prepared electrodes. According to Trasatti *et. al*. (1990), total capacitance can be separated to 2 capacitive elements which are surface capacitance and insertion capacitance. Specific capacitance of leached $LiMn_{2-x}Ti_xO_4$ samples, when x = 0, 0.25, 0.5, 0.75 and 1.00, were collected at different scan speeds from 0.5 to 100 mV s^{-1}. Cyclic voltammograms of leached $LiMn_{2-x}Ti_xO_4$ at different scan rates are shown in Figure 4.11-4.20. Each capacitive element can be determined by plotting the specific capacitance vs inverse square root of scan speed and plot of inverse specific capacitance vs square root of scan speed (Figure 4.21 and Figure 4.22). Figure 4.23 showed insertion (red box), surface capacitance (black box) and total capacitance (red box and black box assemble) of each compound. The results show that total capacitances depend on Ti content. The capacitance decrease continuously when Ti content was increased from x = 0 to x = 0.75 due to the decrease of Mn active species. The capacitance partially increased when x= 1 due to the significant increase of specific surface area. Another possible reason is that the presence of TiO_2 small particles may have decreased the agglomeration of the sample particles and increased the accessible portion of the sample surface (Nia *et al*., 2015). On the other hand, Figure 4.24 shows relation between % insertion capacitance and unit cell parameter change. The difference of % insertion capacitance can be explained by the difference in site occupancy and cell parameters. It was found that % insertion capacitance instantly decreased from x = 0 to x = 0.25, because Ti in spinel MnO_2 induce Mn^{3+} to occupy in 16c site which hinder ion diffusion into the bulk. However, % insertion capacitance increased continuously from x = 0.25 to x = 0.75. Although, Ti content induces the presence of Mn^{3+} in 16c site which hinder ion diffusion in spinel lattice, it also increases unit cell parameter which expands the tunnel and allows more ion to diffuse into the bulk. The effect of larger unit cell parameter due to Ti doping will dominate when x = 0.75. However, % insertion capacitance significantly drops in sample with x = 1 due to the present of TiO_2 rutile impurity. The segregation of TiO_2 rutile could block ion diffusion and decrease the insertion capacitance.

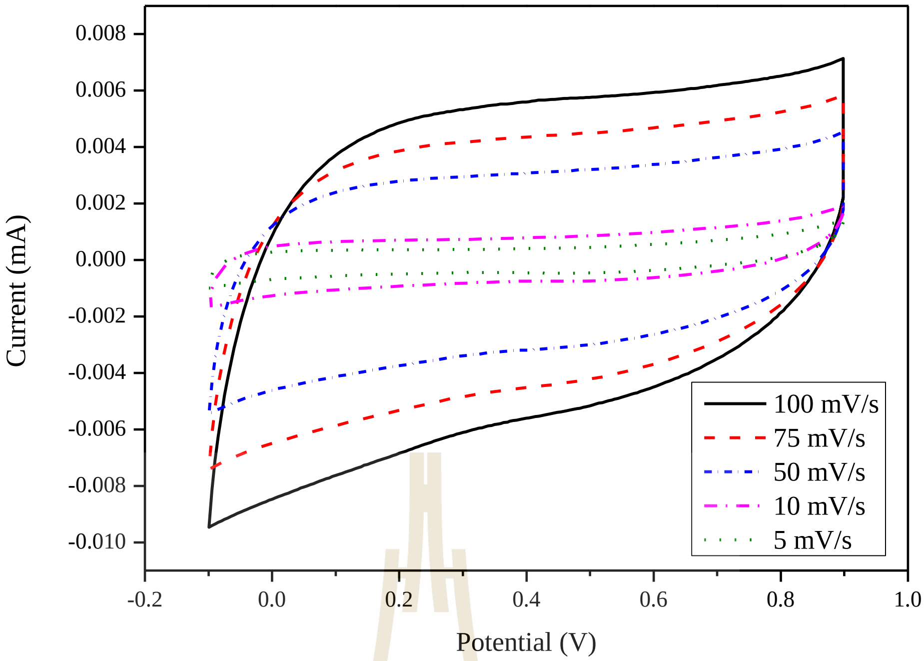

Figure 4.11 Voltammogram of MnO_2 at 5, 10, 50, 75 and 100 mV/s of scan speed.

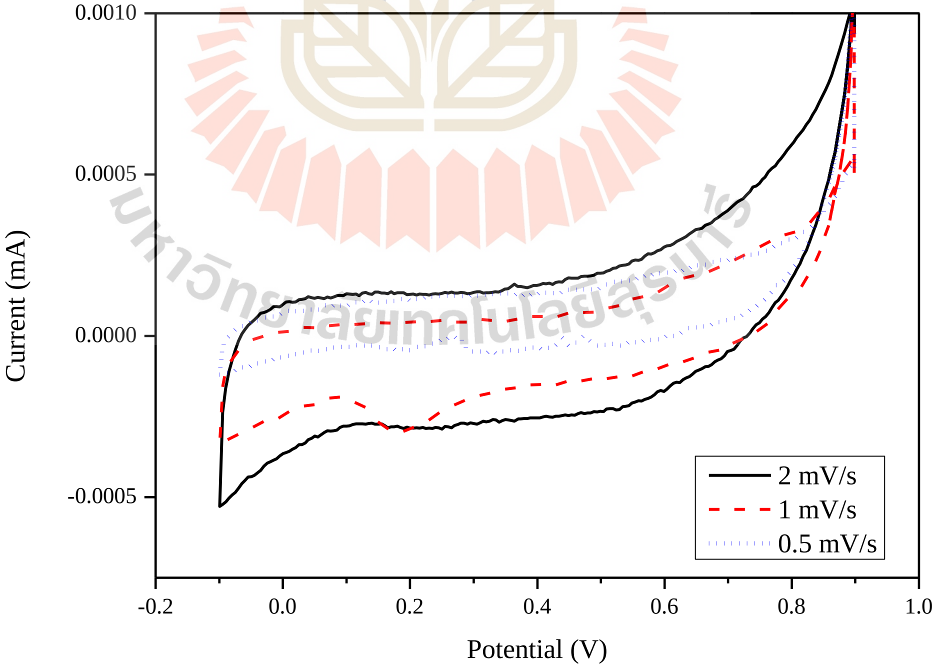

Figure 4.12 Voltammogram of MnO_2 at 0.5, 1 and 2 mV/s of scan speed.

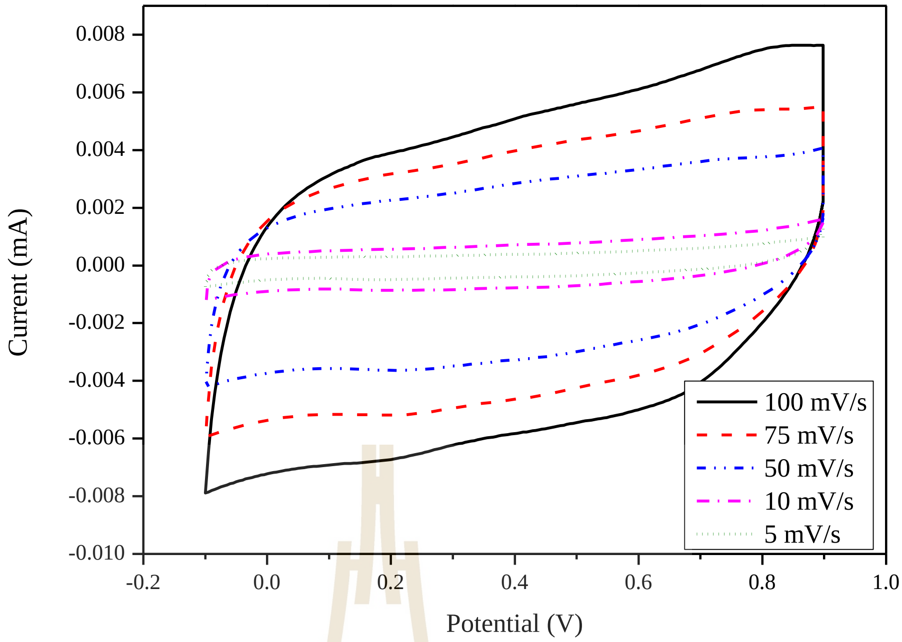

Figure 4.13 Voltammogram of leached $LiTi_{0.25}Mn_{1.75}O_4$ at 5, 10, 50, 75 and 100 mV/s of scan speed.

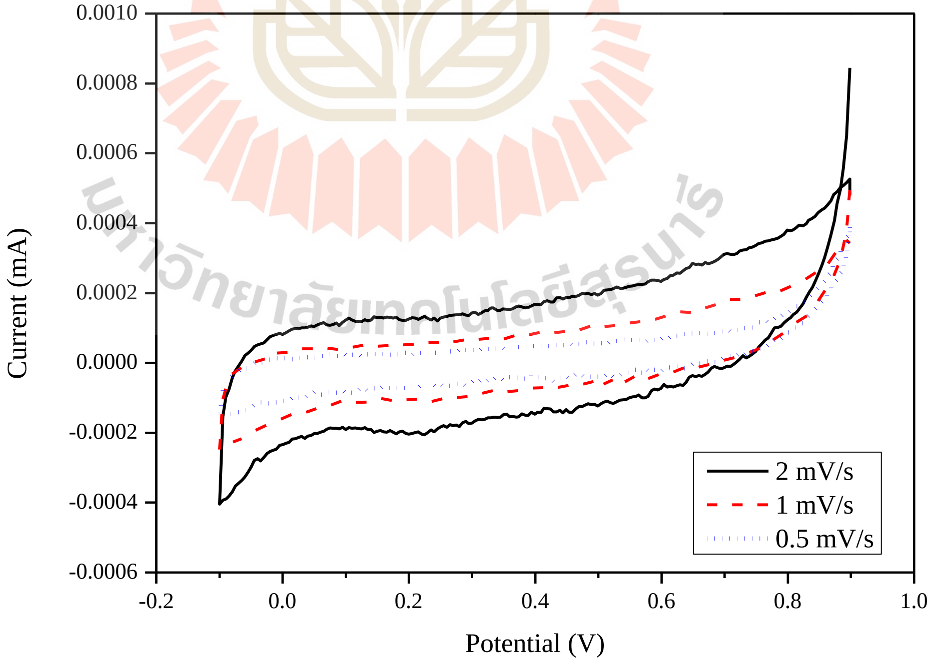

Figure 4.14 Voltammogram of leached $LiTi_{0.25}Mn_{1.75}O_4$ at 0.5, 1 and 2 mV/s of scan speed.

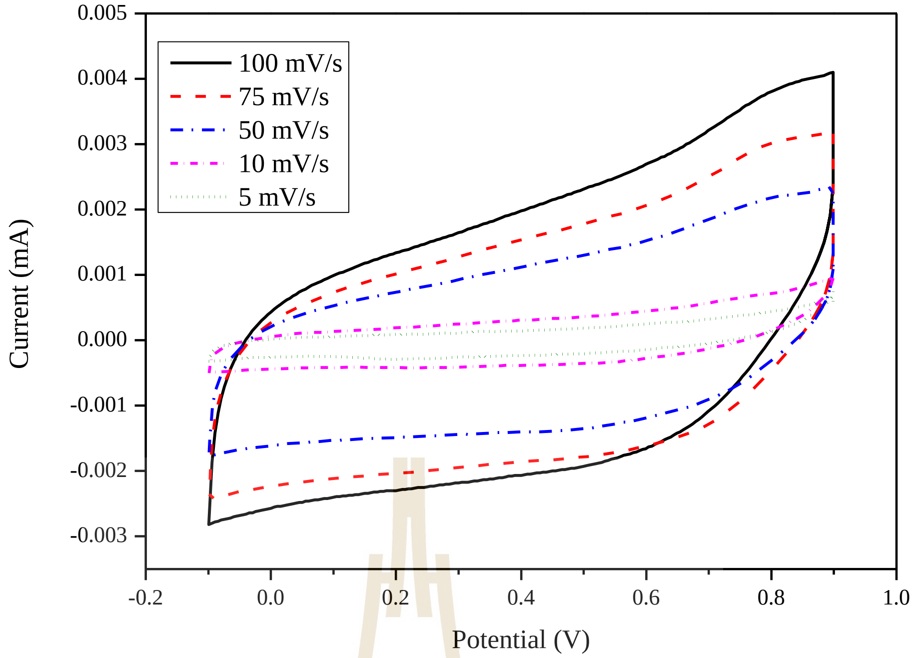

Figure 4.15 Voltammogram of leached $LiTi_{0.5}Mn_{1.5}O_4$ at 5, 10, 50, 75 and 100 mV/s of scan speed.

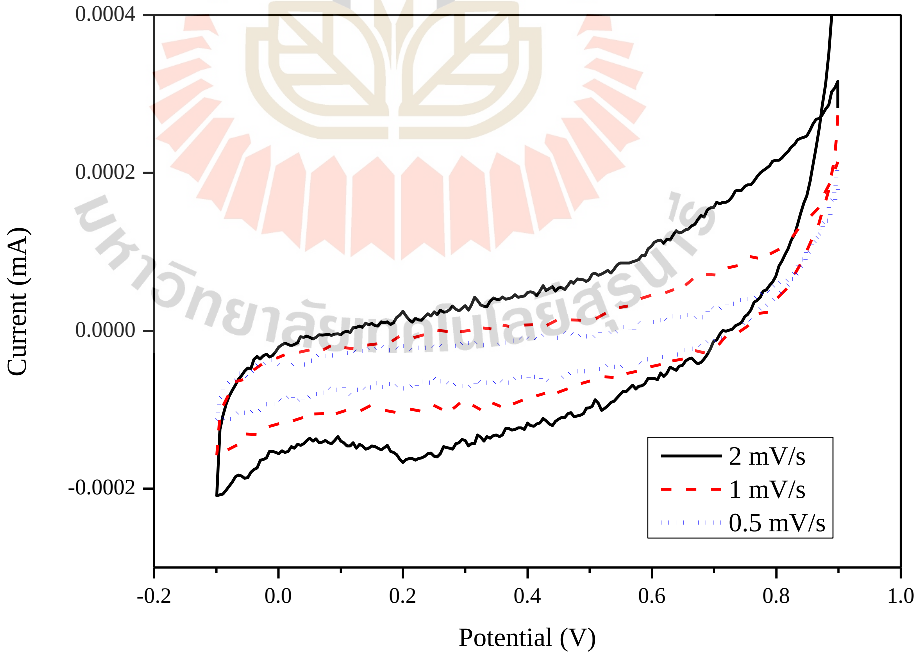

Figure 4.16 Voltammogram of leached $LiTi_{0.5}Mn_{1.5}O_4$ at 0.5, 1 and 2 mV/s of scan speed.

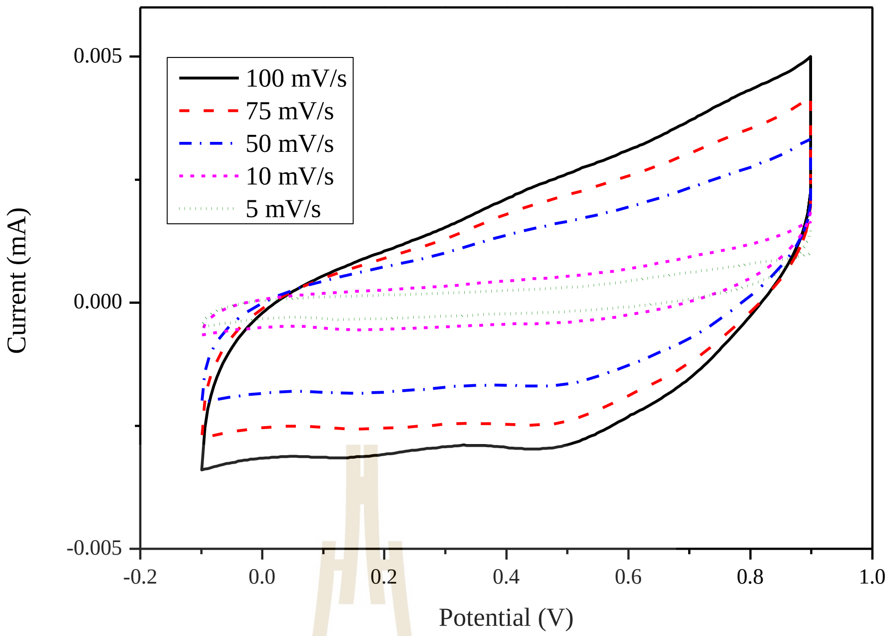

Figure 4.17 Voltammogram of leached $LiTi_{0.75}Mn_{1.25}O_4$ at 5, 10, 50, 75 and 100 mV/s of scan speed.

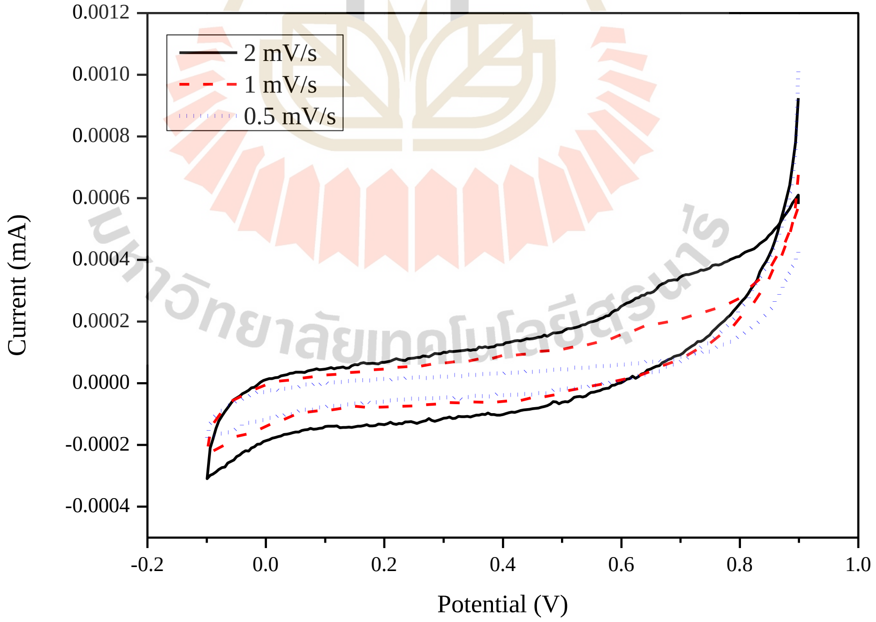

Figure 4.18 Voltammogram of leached $LiTi_{0.75}Mn_{1.25}O_4$ at 0.5, 1 and 2 mV/s of scan speed.

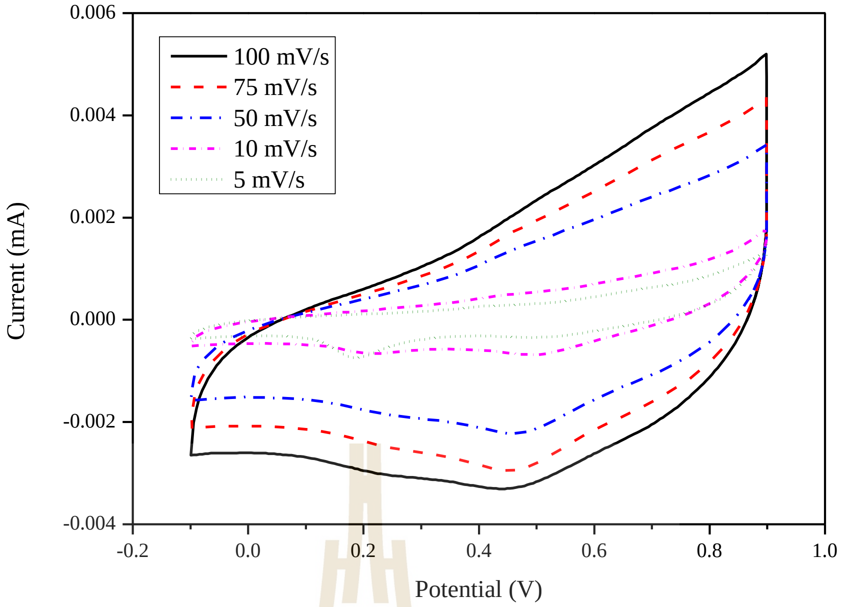

Figure 4.19 Voltammogram of leached $LiTiMnO_4$ at 5, 10, 50, 75 and 100 mV/s of scan speed.

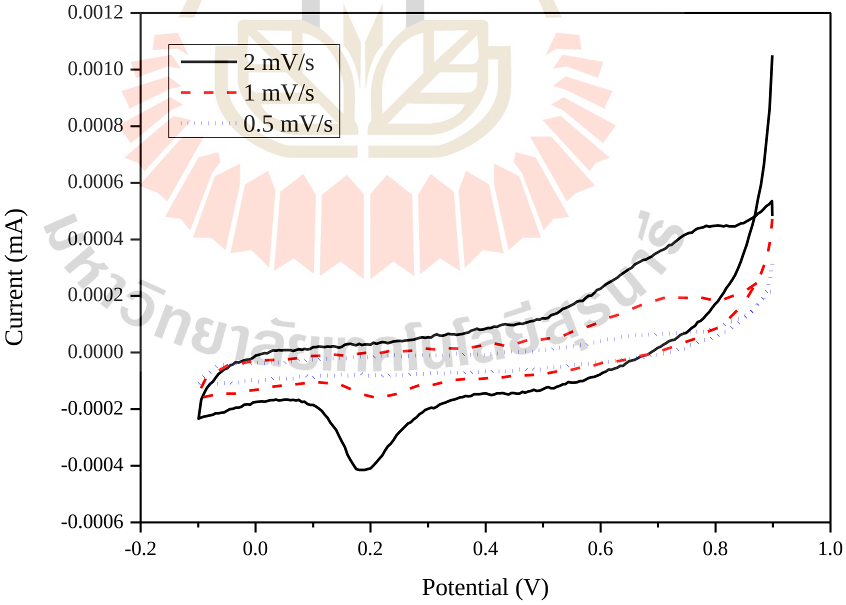

Figure 4.20 Voltammogram of leached $LiTiMnO_4$ at 0.5, 1 and 2 mV/s of scan speed.

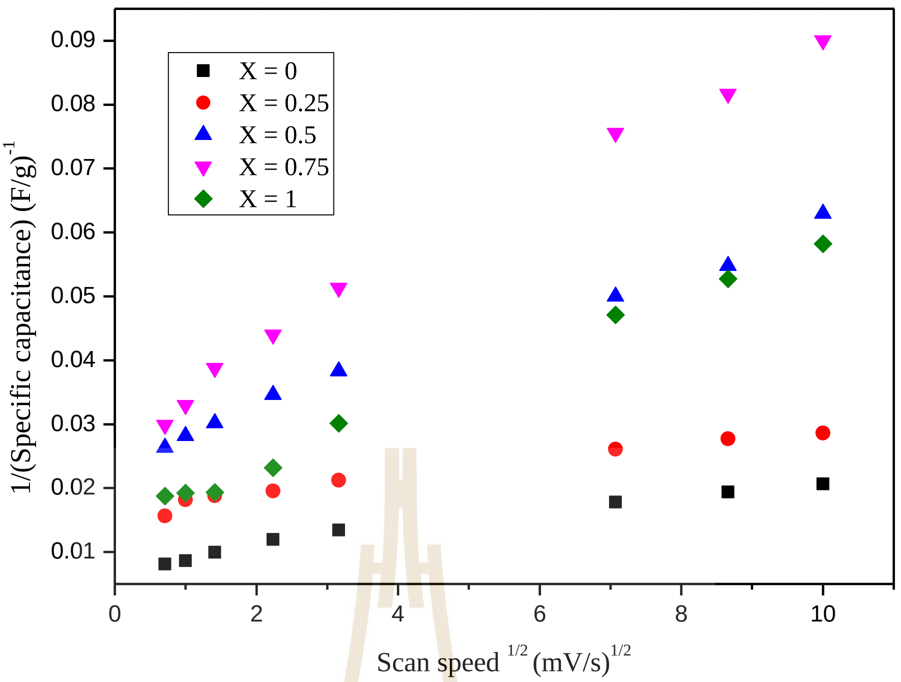

Figure 4.21 Inverse specific capacitance versus square root of scan speed.

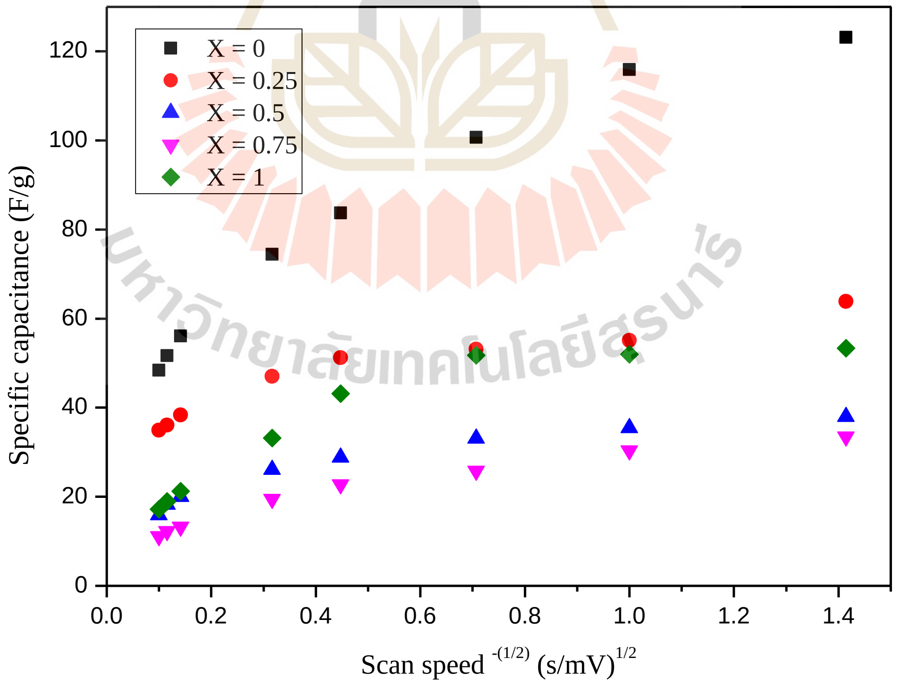

Figure 4.22 Specific capacitance versus inverse square root of scan speed.

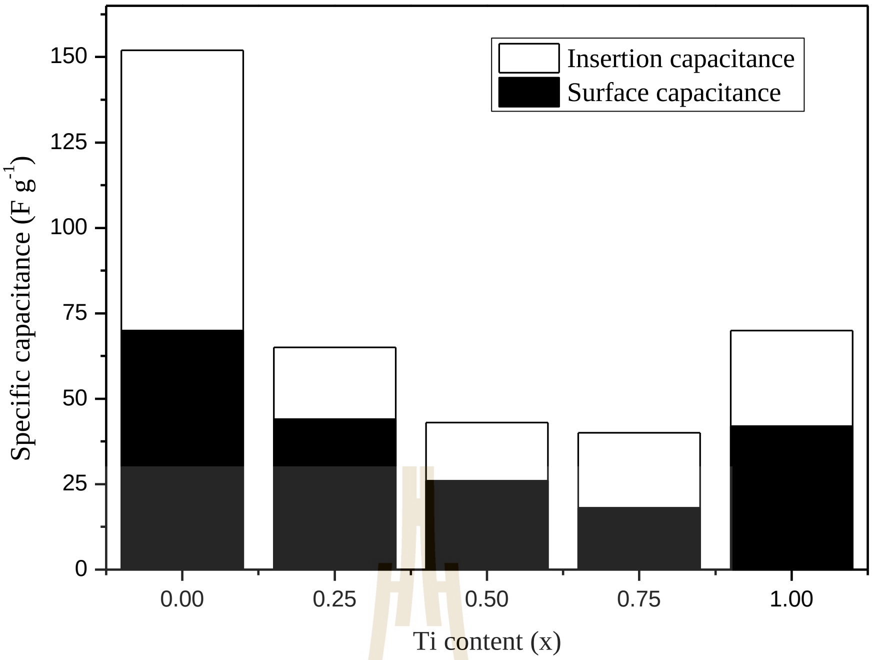

Figure 4.23 Insertion capacitance (red box) and surface capacitance (black box) of leached $LiMn_{2-x}Ti_xO_4$.

.

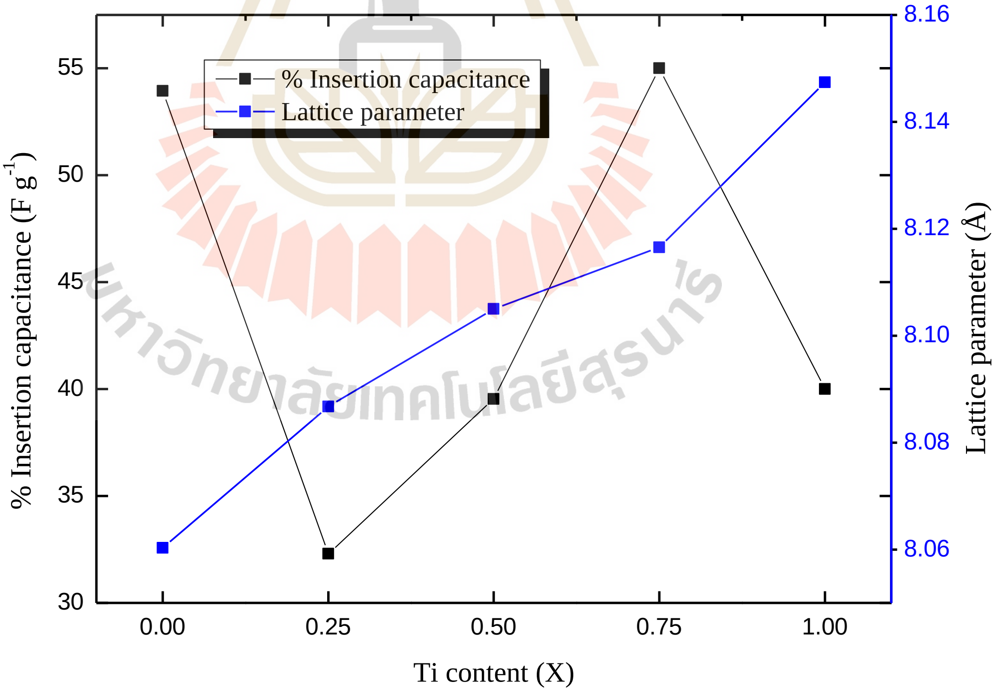

Figure 4.24 Plot of insertion capacitance and unit cell parameter change versus Ti content.

CHAPTER V

CONCLUSIONS

Ti doped MnO_2 spinel have been synthesized via acid treatment of $LiMn_{2-x}Ti_xO_4$. The starting solid solutions of $LiMn_{2-x}Ti_xO_4$ were prepared by solid state reaction at 1073K. X-ray diffraction indicate that the pure phase of spinel is obtained at x = 0, 0.25, 0.5 and 0.75, while TiO_2 rutile impurity is present in a sample with x = 1. XANE spectra show that the oxidation state of Ti and Mn are 4 with a slight mixing of 3+. The oxidation state of Mn is increased after acid leaching. Inductively coupled plasma spectroscopy and energy dispersive X-ray spectroscopy suggest the empirical formula of the products to be $Li_{1-y}Mn_{2-x}Ti_xO_4$. The deintercalation of Li is based on disproportionation of Mn^{3+} and oxidation of Mn^{2+}. In samples with x > 0, it was found that the acid treatment used in this work could not completely remove Li from the structure. X-ray diffraction patterns of $LiMn_{2-x}Ti_xO_4$ indicate the mixed occupancies of Li and another heavy cation between 8a and 16d site in the lattice which could be a reason for an incomplete delithiation. In contrast, after acid treatment, 8a site is occupied by a very small amount of Ti while the remaining Li and some Mn are distributed in 16d and 16c sites. Although Ti clearly affects the crystallographic structure of MnO_2, it has very little effects, if any, on the sample surface morphology and specific surface area.

Cyclic voltammetry was used to study electrochemical behavior of the obtained products. Total capacitance and the surface capacitance are generally affected by the amount of manganese which is the electroactive species. However, the presence of Ti in MnO_2 have two important effects on the crystal lattice. It enlarges the cell parameter and the channel size in the structure while causing some Ti^{4+} and Mn^{3+} to occupy 8a and 16c position. Although the first improves insertion capacitance of the sample, the latter worsens it. The combined effects result in the change of insertion capacitance when Ti content is changed from $x = 0$ to 0.75. TiO_2 impurity in the sample with $x = 1$ cause some deviation from the general trend. While TiO_2 may have additionally contributed to the surface capacitance of the sample giving rise to the unexpectedly high value, they most likely block ion diffusion to the bulk and consequently lower its insertion capacitance.

REFERENCES

REFERENCES

Ardizzone, S., Fregonara, G. and Trasatti, S. (1990). Inner and outer active surface of RuO_2 electrodes. **Electrochimica Acta.** 35: 263.

Avdeev, G., Amarilla, J. M., Rojo, J. M., Petrov, K. and Rojas, R. M. (2009). Composition and structure of acid leached $LiMn_{2-y}Ti_yO_4$ ($0.2 \leq y \leq 1.5$) spinels. **Journal of Solid State Chemistry**. 182(12): 3226-3231.

Balzarotti, A. (1980). K-edge absorption of titanium in the perovskites $SrTiO_3$, $BaTiO_3$ and TiO_2. **Solid State Communications**. 35(2): 145-149.

Ben. (2006). Molecular geometry [On-line] Available: https://commons.wikimedia.org/wiki/File:Octahedral-3D-balls.png.

Chen, K., Pan, W. and Xue, D. (2016). Phase transformation of Ce^{3+}-doped MnO_2 for pseudocapacitive electrode materials. **The Journal of Physical Chemistry C**. 120(36): 20077-20081.

Devaraj, S. and Munichandraiah, N. (2008). Effect of crystallographic structure of MnO_2 on its electrochemical capacitance properties. **The Journal of Physical Chemistry C**. 112: 4406-4417.

Ghodbane, O., Ataherian, F., Wu, N.-L. and Favier, F. (2012). In situ crystallographic investigations of charge storage mechanisms in MnO_2-based electrochemical capacitors. **Journal of Power Sources**. 206: 454-462.

Ghodbane, O., Pascal, J. L. and Favier, F. (2009). Microstructural effects on charge-storage properties in MnO_2-based electrochemical supercapacitors. **ACS Appl Mater Interfaces**. 1(5): 1130-1139.

Guler, M. O., Akbulut, A., Cetinkaya, T., Uysal, M. and Akbulut, H. (2014). Improvement of electrochemical and structural properties of $LiMn_2O_4$ spinel based electrode material for Li-ion batteries. **Internatioal Journal of Hydrogen Energy**. 39: 21447-21460.

Hunter, J. C. (1981). **Journal of Solid State Chemistry**. 39: 142.

Rietveld, H. M. (1967). **Acta Crystallography**. 22: 157.

Jayalakshmi, M. and Balasubramanian, K. (2008). Simple capacitors to supercapacitors - an overview. **International Journal of Electrochemical Science**. 3: 1196-1217.

Krins, N., Hatert, F., Traina, K., Dusoulier, L., Molenberg, I., Fagnard, J. and Vertruyen, B. (2006). $LiMn_{2-x}Ti_xO4$ spinel-type compounds ($x \leq 1$): Structural, electrical and magnetic properties. **Solid State Ionics**. 177(11-12): 1033-1040.

Li, D., Li, W., Deng, Y., Wu, X., Han, N. and Chen, Y. (2016). Effective Ti doping of δ-MnO_2 via anion route for highly active catalytic combustion of benzene. **The Journal of Physical Chemistry C**. 120(19): 10275-10282.

Liu, H. and Zhu, G. (2007). The electrochemical capacitance of nanoporous carbons in aqueous and ionic liquids. **Journal of Power Sources**. 171(2): 1054-1061.

Luo, J. Y. and Xia, Y. Y. (2007). Effect of pore structure on the electrochemical capacitive performance of MnO_2. **Journal of The Electrochemical Society**. 154(11): A987-A992.

Ma, L. W., Chen, B. Z., Shi, X. C., Zhang, W. and Zhang, K. (2010). Stability and Li^+ extraction/adsorption properties of $LiM_xMn_{2-x}O_4$ (M=Ni, Al, Ti; 0≤x≤1) in aqueous solution. **Colloids and Surfaces A: Physicochemical and Engineering Aspects**. 369(1-3): 88-94.

Mao, L., Zhang, K., On Chan, H. S. and Wu, J. (2012). Nanostructured MnO_2/graphene composites for supercapacitor electrodes: the effect of morphology, crystallinity and composition. **Journal of Materials Chemistry**. 22(5): 1845-1851.

Murphy, D. T., Schmid, S., Hester, J. R., Blanchard, P. E. and Miiller, W. (2015). Coordination site disorder in spinel-type LiMnTiO4. **Inorganic Chemistry**. 54(10): 4636-4643.

Nia, M. H., Rezaei-Tavirani, M., Nikoofar, A. R., Masoumi, H., Nasr, R., Hasanzadeh, H. and Shadnush, M. (2015). Stabilizing and dispersing methods of TiO_2 nanoparticles in biological studies. **Journal of Paramedical Sciences**. 6: 96-105.

Pandolfo, A. G. and Hollenkamp, A. F. (2006). Carbon properties and their role in supercapacitors. **Journal of Power Sources**. 157(1): 11-27.

Pargoletti, E., Cappelletti, G., Minguzzi, A., Rondinini, S., Leoni, M., Marelli, M. and Vertova, A. (2016). High-performance of bare and Ti-doped α-MnO_2 nanoparticles in catalyzing the oxygen reduction reaction. **Journal of Power Source.** 325: 116-128.

Petrov, K., Rojas, R. M., Alonso, P. J., Amarilla, J. M., Lazarraga, M. G. and Rojo, J. M. (2005). Cation distribution and phase transformations in $LiMn_{2-y}Ti_yO_4$ solid solutions. **Solid State Sciences**. 7(3): 277-286.

Ragupathy, P., Park, D. H., Campet, G., Vasan, H. N., Hwang, S.-J., Choy, J.-H. and Munichandraiah, N. (2009). Remarkable capacity retention of nanostructured manganese oxide upon cycling as an electrode material for supercapacitor. **The Journal of Physical Chemistry C**. 113: 6303-6309.

Ragupathy, P. V. and Munichandraiah, N. (2008). Synthesis and characterization of nano-MnO_2 for electrochemical supercapacitor studies. **Journal of Electrochemical Society**. 155: A34-A40.

Sawangphruk, M. and Limtrakul, J. (2012). Effects of pore diameters on the pseudocapacitive property of three-dimensionally ordered macroporous manganese oxide electrodes. **Materials Letters**. 68: 230-233.

Zurek, S. (2014). Ragone plot. [On-line] Available: https://commons.wikimedia.org/wiki/File:Supercapacitors_chart.svg.

Subramanian, V., Zhu, H., Vajtai, R., Ajayan, P. M. and Wei, B. (2005). Hydrothermal synthesis and pseudocapacitance properties of MnO_2 nanostructures. **The Journal of Physical Chemistry B**. 109: 20207-20214.

Sung, D.-Y., Kim, I. Y., Kim, T. W., Song, M.-S. and Hwang, S.-J. (2011). Room temperature synthesis routes to the 2D nanoplates and 1D nanowires/nanorods of manganese oxides with highly stable pseudocapacitance behaviors. **The Journal of Physical Chemistry C**. 115(27).

Tarascon, J. M. (1991). The spinel phase of $LiMn_2O_4$ as a cathode in secondary lithium cells. **Journal of The Electrochemical Society**. 138(10): 2859.

Uberuaga, B. P., Tang, M., Jiang, C., Valdez, J. A., Smith, R., Wang, Y. and Sickafus, K. E. (2015). Opposite correlations between cation disordering and amorphization resistance in spinels versus pyrochlores. **Nature Communications**. 6: 8750.

Vu, N. H., Arunkumar, P., Won, S., Kim, H. J., Unithrattil, S., Oh, Y. and Im, W. B. (2017). Effects of excess Li on the structure and electrochemical performance of $Li_{1+z}MnTiO_{4+\delta}$ cathode for Li-ion batteries. **Electrochimica Acta**. 225: 458-466.

Wan, C., Yuan, L. and Shen, H. (2014). Effects of electrode mass-loading on the electrochemical properties of porous MnO_2 for electrochemical supercapacitor. **International Journal of Electrochemical Science.** 9: 4024-4038.

Wang, H.-Q., Lai, F.-Y., Li, Y., Zhang, X.-H., Huang, Y.-G., Hu, S.-J. and Li, Q.-Y. (2015). Excellent stability of spinel $LiMn_2O_4$-based cathode materials for lithium-ion batteries. **Electrochimica Acta**. 177: 290-297.

Wang, S., Yang, J., Wu, X., Li, Y., Gong, Z., Wen, W. and Yang, Y. (2014). Toward high capacity and stable manganese-spinel electrode materials: A case study of Ti-substituted system. **Journal of Power Sources**. 245: 570-578.

Wang, Y., Chen, L., Wang, Y. and Xia, Y. (2015). Cycling stability of spinel $LiMn_2O_4$ with different particle sizes in aqueous electrolyte. **Electrochimica Acta**. 173: 178-183.

Wu, C., Wu, F., Chen, L. and Huang, X. (2002). X-ray diffraction and X-ray photoelectron spectroscopy analysis of Cr-doped spinel $LiMn_2O_4$ for lithium ion batteries. **Solid State Ionics**. 152-153: 335-339.

Xie, Y., Xu, Y., Yan, L., Yang, Z. and Yang, R. (2005). Synthesis and electrochemical properties of Sc-doped LiScMnO spinel as cathodic material for rechargeable Li-battery. **Solid State Ionics**. 176(35-36): 2563-2569.

Zhang, X., Sun, X., Zhang, H., Li, C. and Ma, Y. (2014). Comparative performance of birnessite-type MnO_2 nanoplates and octahedral molecular sieve (OMS-5) nanobelts of manganese dioxide as electrode materials for supercapacitor application. **Electrochimica Acta**. 132: 315-322.

Zhang, X., Yang, M., Zhao, X., Wang, Y., Wang, M. and Ma, L. (2015). The spinel phase $LiMnTiO_4$ as a potential cathode for rechargeable lithium ion batteries. **Journal of Materials Science: Materials in Electronics**. 26(9): 6366-6372.

Zhang, Y., Feng, H., Wu, X., Wang, L., Zhang, A., Xia, T. and Zhang, L. (2009). Progress of electrochemical capacitor electrode materials: A review. **International Journal of Hydrogen Energy**. 34(11): 4889-4899.

Zhi, M., Xiang, C., Li, J., Li, M. and Wu, N. (2013). Nanostructured carbon-metal oxide composite electrodes for supercapacitors: a review. **Nanoscale**. 5(1): 72-88.

CURRICULUM VITAE

Name Mr. Paradron Lektrakoontara

Date of Birth Juner 18th, 1991, Khonkaen, Thailand

Address 76/3 moo.4 Sirchan rd. Naimuang sub district, Muang district
Khonkaen 40000

Education

2010-2013 B.Sc. (Chemistry), Khonkaen University, Thailand

2014-2017 Student at department of chemistry, Suranaree University of Technology, Thailand